Journal of Materials Chemistry A

Accepted Manuscript

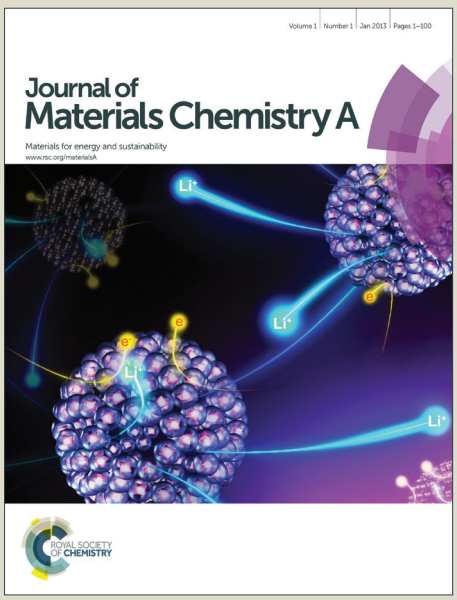

ROYAL SOCIETY OF CHEMISTRY

www.rsc.org/materialsA

Perovskite-Based Solar Cells: Impact of Morphology and Device Architecture on Device Performance

Teddy Salim,[a] Shuangyong Sun,[a] Yuichiro Abe,[a,b] Anurag Krishna,[a,b] Andrew C. Grimsdale[a] and Yeng Ming Lam[a*]

[a] School of Materials Science and Engineering, Nanyang Technological University, 50 Nanyang Avenue, 639798, Singapore

[b] Energy Research Institute @ NTU (ERI@N), Nanyang Technological University, Research Techno Plaza, Singapore 637553 637141, Singapore

* Corresponding author: ymlam@ntu.edu.sg

Abstract

Organic-inorganic metal halide perovskite has recently shown great potential for applications in solar cells with excitingly high performances with an up-to-date NREL-certified record efficiency of 20.1%. This family of materials has demonstrated considerable prospects in achieving comparable or even better efficiencies than those of thin film solar cells. The remarkable performances thus far seem not to be limited to any specific device architecture. Both mesoscopic and planar cells showed good device performance and this eventually leads to the inevitable comparison between both architectures. Regardless of device architecture, device performance is highly dependent on the film morphology. The factors influencing the film morphology such as the deposition method, material composition, additives and film treatment will be discussed extensively in this review. The key to obtaining good-quality film morphology

and hence performance is to essentially lower the energy barrier for nucleation and to promote uniform growth of the perovskite crystals. A comparison of the material selection for the various layers as well as their corresponding impact on the perovskite film and device behavior in both device architectures will be presented.

1. Introduction

The use of organic-inorganic metal halide perovskites in optoelectronic devices, such as field effect transistors and optical devices, is not new.[1-3] That being said, the viability of this class of material for solar-to-electrical power conversion was only demonstrated in 2009 by Kojima *et al*.[4] Ever since then, there is no looking back for these perovskites based solar cells. The power conversion efficiency (PCE) of solar cells based on methylammonium lead halide ($CH_3NH_3PbX_3$ where X can be I, Br or Cl) has increased dramatically from the initial 3.9% to more than 19%[5] in a short span of less than 5 years. In comparison, multicomponent chalcogenide thin-film solar cells, such as $CuIn_xGa_{1-x}Se_2$, took 35 years to achieve similar improvement in efficiency. More interestingly, the good performance so far seems not to be confined to a single type of ideal architecture. Both mesoscopic solar cells (similar to solid state dye-sensitized solar cells) and planar heterojunction (PHJ) solar cells have shown impressive efficiencies. On top of this, there is a wide range of techniques, ranging from solution to vacuum based, that can be used for the fabrication of highly efficient devices with either architecture. It is precisely the robustness of the devices demonstrated so far that has convinced both scientific and industrial communities that the efficiencies can be further improved if there is a better understanding on how optimal processing conditions are related to the device architectures and how this in turn affects the device performance.

Organic-inorganic metal halide perovskites, specifically methylammonium lead iodide ($CH_3NH_3PbI_3$), was initially utilized as sensitizer for liquid-state dye-sensitized solar cells in the form of nanoparticles decorating the surface of a mesoporous metal oxide film.[4,6] Though reasonable PCE was achieved when coupled with a iodide/triiodide liquid electrolyte, the stability of the cells was poor due to the dissolution of the perovskite layer. A breakthrough moment for these mesoscopic solar cells came in 2012 when the perovskite was coupled with organic small molecule – 2,2',7,7'-tetrakis(*N,N*-di-*p*-methoxyphenyl-amine)-9,9'-spirobifluorene (spiro-OMeTAD) as the hole transport material (HTM) analogous to a solid state dye sensitized cell (DSSC).[7,8] Kim *et al.* showed $CH_3NH_3PbI_3$ solar cells with titanium oxide (TiO_2) scaffold could result in a PCE of up to 9.7%.[8] Transient absorption studies of these cells revealed that holes were injected from $CH_3NH_3PbI_3$ into spiro-OMeTAD following the electron transfer from the perovskite phase to mesoscopic TiO_2 film. Since the TiO_2 scaffold participates in the photoconversion process, it can be considered an active component in the perovskite solar cell; hence we designate TiO_2 and metal oxides with similar functions as "*active scaffolds*".

During the same period, Lee *et al.* demonstrated a variation from these "active scaffolds" mesoscopic cells. Mixed halide perovskite ($CH_3NH_3PbI_{3-x}Cl_x$) was deposited on an insulating aluminum oxide (Al_2O_3) scaffold and this is coupled to spiro-OMeTAD. With this configuration, an impressive PCE of 10.9% could be achieved. This type of solar cells are now more commonly known as meso-superstructured solar cell (MSSC).[7] In MSSCs, the methyl ammonium lead halide acted as both sensitizer and electron transport material (ETM). The metal oxides in MSSCs only function as the scaffold and electrons could not be injected into the insulating Al_2O_3 layer due to its wide bandgap. Since these insulating mesoporous metal oxide films do not participate actively in the charge transport and only act purely as a supporting scaffold for

perovskite, it is considered as a "*passive scaffold*" (or inactive scaffold). In general, regardless of whether the scaffold is active or passive, thicker and more uniform perovskite films can be deposited on these scaffolds. This in turn is translated to higher light absorption and improved electrical properties for these cells.

The other organic-inorganic metal halide-based solar cell device architecture that coexists symbiotically with the mesoscopic structure discussed above is the planar heterojunction (PHJ) architecture. In this configuration, a semiconducting absorber is typically sandwiched between two selective contacts in the absence of mesoporous (or nanoporous) scaffold. This type of architecture possesses a more discernible interface between layers, which consequently provides a more straightforward platform for fundamental investigations of materials properties and device physics. Charge-selective transporting (or blocking) layers are often employed in planar devices, just as in to the mesoscopic solar cells. This "stacked-layer" architecture is also widely encountered in thin-film solar cells and, to a certain extent, in organic solar cells.[9,10]

In early work performed by Ball *et al.*, planar devices based on mixed halide $CH_3NH_3PbI_{3-x}Cl_x$ perovskite only yielded PCE of 4.9%, while the corresponding devices with the incorporation of mesoporous Al_2O_3 scaffold were more than twice as efficient.[11] Nevertheless, the following revelations pertaining to the material properties of these hybrid halide material: (1) the combination of both high dielectric constant and low effective masses in hybrid halide perovskite promotes the formation of Wannier-Mott excitons, *i.e.*, a type of exciton with low binding energies and high likelihood to dissociate in bulk even at room temperature;[12] (2) electron–hole diffusion lengths are long (exceeding 100 nm) and balanced;[13,14] (3) high optical absorptivity of organolead halide perovskite enables efficient photon harvesting even with an ultrathin absorber layer,[15,16] suggest that it is conceptually viable to obtain highly efficient perovskite solar cells

with a thin-film planar architecture. Thus despite the sluggish start, planar heterojunction perovskite solar cells were soon found to catch up with the performance of the mesoscopic ones. Device efficiencies in excess of 15% – even as high as 19.3%, although most of these remain uncertified, exhibit the immense potential in these thin-film planar heterojunction perovskite solar cells.[5,17-25]

Organometal halide perovskite-based solar cells have presented to the solar cells community not only an exciting but also a challenging problem. The euphoria is mainly because of the incredibly high efficiencies achieved so far; those exceptional results are not only limited to a few groups with special facilities, instead they have been reproduced by different research groups all over the world. On the other hand, it is challenging because of the incredibly fast pace at which the efficiency is evolving, which divert the attention away from fundamental studies of these perovskite materials, their interfaces with the other layers and the impact of the device architectures on the morphologies of the films. In this review, an attempt is made to discuss various strategies to control the morphology of organometal halide perovskites. Together with this, the common architectures employed in perovskite-based solar cells and how they dictate the choice of interlayers and device performances are also presented. Other review papers on similar topic have been published earlier by Gamliel and Etgar and by He *et al*.[26,27] We distinguish our work in terms of the extent of the scope covered as well as the insights provided on the relevant studies to date.

2. Morphological control

In order to get good performance in planar perovskite devices, the most direct approach implemented by different groups thus far is to increase the thickness of the organolead halide

perovskite layer to maximize photon harvesting. However, this is not as straightforward as it seems because the film quality and hence the shunting pathways and the absorption quality of the device are related to its crystallization behaviour. Therefore, one of the main challenges in this field is the fabrication of high quality films with controlled morphology, high surface coverage and minimum pinholes for high performance, solution-processed thin-film perovskite devices. Factors such as charge dissociation efficiency, charge transport and diffusion length of charge species are dependent on the crystallinity of the film.[14,28] The crystallization behaviour of these perovskite materials in turn is highly dependent on factors such as deposition methods, composition, type of surfaces (surface chemistry, degree of hydrophilicity, surface structure, *etc*.), and solvents/additives used. Until recently, humidity was shown to be detrimental to the performance of the cells[28] because of the hygroscopic nature of $CH_3NH_3^+$ but it was found that controlled humidity of about 30% was able to help with the reconstruction during the film formation process by partially dissolving the reactant species. This gives rise to a spectacular efficiency of more than 19%[5] which enables these cells to compete with conventional thin-film solar cells.

In the case of mesoscopic solar cells, the mesopores, regardless of whether if it is TiO_2, Al_2O_3 or NiO, provide a physical constraint on the crystals dimensions. This resulted in the possibility of achieving good film quality even with reasonably thick film. This is the reason for the excellent device performance obtainable with this architecture.[29] One important point to note in the mesoscopic devices, a perovskite overlayer is still necessary for good device performance.[11] The crystals within the perovskite overlayer have a much larger grain size (100–1000 nm), which is necessary for better charge transport. Ball *et al.* demonstrated clearly that the crystal size of the mixed halide organolead perovskite $CH_3NH_3PbI_{3-x}Cl_x$ was reduced to less than 100 nm in

mesoporous Al_2O_3 compared to planar system in which the crystals can be more than 500 nm in size. This results in an increase in the J_{SC} for the planar device as there is less charge trapping and recombination at grain boundaries (V_{OC} and FF are better with the MSSCs because of the better film formation and hence reduced in shunting paths).[11] This is contradictory to an earlier work published by Lee *et al.* from the same research group claiming that the optimized device is one without capping layer.[7] The reason for this discrepancy is most probably because of the different conditions for the processing of Al_2O_3. In the previous paper by Lee *et al*., the sintering temperature of Al_2O_3 was 500 $^{\circ}$C but in the latter paper by Ball *et al.*, the temperature was lowered to 150 $^{\circ}$C. The crystallization behaviour is most likely different due to the difference in the surface energy of the Al_2O_3 scaffolds annealed at different temperatures.

Due to the sensitivity of perovskite-based solar cells to its film morphology, controlled crystallization is an essential consideration in the fabrication of these cells. Crystallization is a complex process that involves two main steps – nucleation and growth. Nucleation from a continuous phase can occur homogeneously or heterogeneously. The classical theory arises from the work by Gibbs, Volmer and others.[30] Homogeneous nucleation is a matter of considering the overall excess free energy. On the other hand, heterogeneous nucleation, which occurs on foreign nuclei or surfaces, imposes a consideration of surface or interface contact energy due to the wetting on foreign surfaces. Therefore factors affecting surface properties, such as chemistry of the surfaces – types of materials (TiO_2 *vs*. Al_2O_3 or PEDOT:PSS), thermal treatment on surfaces, surface morphology (mesoporous *vs.* compact layer) – become very important in addressing this type of nucleation. Nucleation barrier is much lower for heterogeneous nucleation compared to homogeneous nucleation because of the shape of the nucleus. The free energy needed for heterogeneous nucleation ($\Delta G_{heterogeneous}$) is related to that needed for homogeneous nucleation

($\Delta G_{homogeneous}$) by the following expression and the terms are defined in the schematic shown in Fig. 1:

$$\Delta G_{heterogeneous} = \Delta G_{homogeneous} \times f(\theta)$$

where $f(\theta) = \frac{2-3\cos\theta+cos^3\theta}{4}$.

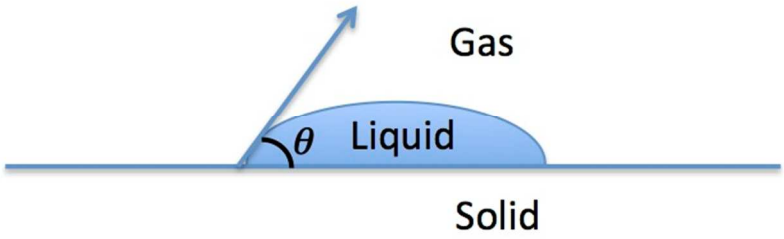

Fig. 1 Simplified schematic of heterogeneous nucleation on solid surfaces.

This essentially means that the energy barrier for heterogeneous nucleation on solid/liquid interfaces is lower than that for homogeneous nucleation. Better wetting (smaller contact angle, θ) will lower the nucleation barrier. It is consequently expected that nucleation and hence growth of perovskite crystals will occur more easily when the solution is deposited on substrates with higher surface area or more hydrophilic since perovskite materials are generally dissolved in more polar solvents such as γ-butyrolactone (GBL), *N,N*-dimethylformamide (DMF) and dimethylsulfoxide (DMSO). On top of this, in the case of mesoporous scaffold, regardless if the scaffold participates in the electron transport, the curvature is towards the liquid, the contact angle will be further reduced and hence further reducing the energy barrier. The contradictory results presented by Lee *et al.* and Ball *et al.* can therefore be explained by the differences in the crystallization process due to the variation in surface properties.[7,11] Dehydroxylation of the Al_2O_3

surface occurs upon heating of Al_2O_3 to above 500 °C rendering the surface less hydrophilic.[31] This increases the barrier for nucleation. Therefore, one of the criteria for uniform morphology is to encourage of heterogeneous nucleation to happen and this can be done with the use of mesoporous scaffold (large surface area) and making the surface hydrophilic (reduce dehydroxylation on oxide film).

For both mesoscopic and planar architectures, a variety of methods have been demonstrated to control the growth kinetics of the perovskite film. Factors such as solution concentration, precursor ratio, solvent, deposition temperature and film-substrate interfacial interaction are found to affect the film formation.[32] As mentioned earlier, pinholes and incomplete surface coverage of a perovskite film in a device may result in low-resistance shunting pathways (*via* direct contact of *n*-type electron-transporting layer and *p*-type hole-transporting layer) and contribute to loss in photon absorption; both are detrimental to the device performance. Therefore, effective ways to manipulate nucleation and growth of perovskite crystals in solution-processed system, particularly in planar system, in order to achieve optimum film morphology are highly sought after. The following are a few strategies that have been adopted to control the morphology of perovskite films.

2.1 Deposition methods

The morphology of organometal halide perovskite, which essentially comprises two main precursor components, depends on the deposition route (solution-based or vacuum-based). The precursors can either be simultaneously or independently deposited. The combination of these permutations generates a range of thin-film deposition techniques for hybrid perovskite materials. In general, without any additional confinement, or any modification to the

composition or alteration to the crystallization process, single deposition produces a more uncontrollable crystallization resulting in a variety of morphology and hence a spectrum of device performance. In single deposition approach, a mixture of metal halide and organohalide of certain ratio, typically dissolved in a common solvent and spincoated on a substrate.[8] This approach is the most cost effective and straightforward to implement. Nevertheless, efficiencies of planar devices prepared with this method are usually limited, owing to poor film formation (incomplete surface coverage with pinholes) induced by extensive crystallization caused by solvent evaporation and strong ionic interaction between the metal cations and the halides.[33,34] The choice of effective solvent capable of simultaneously dissolving both precursors is also limited. In our previous work, we managed to obtain PCE as high as 5.2% with an inverted PEDOT:PSS/$CH_3NH_3PbI_3$ (50 nm)/$PC_{61}BM$ by employing one-step solution approach.[15] However obtaining thicker but smooth and uniform films by spincoating solutions of higher concentrations was a challenge.

Sequential deposition method offers the possibility of a more controlled crystallization of perovskite.[28,35] Metal halide (*e.g.*, PbI_2) is first introduced in the mesoporous TiO_2 scaffold; at a relatively high concentration, PbI_2 in the form of hexagonal 2H polytype is constrained by the pores (~ 22 nm). Upon exposure to the other organohalide (*e.g.,* CH_3NH_3I) precursor solution, the conversion to perovskite occurs immediately within seconds. On the other hand, the conversion takes longer for on a planar substrate, *i.e.*, incomplete conversion was observed even after 45 min. In planar system, MAI needs to diffuse into the PbI_2 film prior to conversion. Perovskite crystallization becomes kinetically more controllable because nucleation and reaction rate between both precursors can be independently manipulated. An additional heat treatment is performed to remove residual solvent and to promote a more complete conversion. This

technique enables highly efficient mesoscopic perovskite solar cell device (PCE = 15%) with improved reproducibility. We have also implemented this strategy for inverted planar device, resulting in improved efficiency from 5.2% to 7.4%.[15] The success of sequential deposition was also observed by Hu *et al*., who employed the method in fabricating NiO-based inverted planar perovskite solar cell.[36] They claimed that the metal halide film had to be first heated before being dipped into a warm (70 ℃) organohalide solution. The sequentially deposited CH_3NH_3I film exhibited large crystals on the length scale of tens of nanometers. The other variation of the two-step solution-based deposition was demonstrated by Xiao *et al*.[19] where a bilayer of each component was deposited on top of each other and heated to encourage the interdiffusion of both precursor materials. The degree of conversion depends on the amount of precursors available (PbI_2/CH_3NH_3I thickness ratio in the bilayer film), temperature and duration of the heat treatment. The optimized device showed an efficiency of 15.4% with high reproducibility and no obvious hysteresis. The method was further modified by Chiang *et al.* who spincoated 4 times as slowly and the resulting film required no heating.[22] The slower spincoating prevented rapid solvent removal, which in turn assisted the infiltration of CH_3NH_3I molecules into PbI_2 film. They successfully obtained planar device with remarkable conversion efficiency of 16.3% with no hysteresis observed.

Vacuum-based deposition offers potential solutions to the limitations imposed by solution processing. Liu *et al.* used a dual-source vapor deposition technique to prepare mixed halide $CH_3NH_3PbI_{3-x}Cl_x$ perovskite thin film.[17] The film had extremely high uniformity over a range of length scales on compact TiO_2 with crystalline features on the length scale of hundreds of nanometers. As a result, the vapor-deposited sample yielded high PCE of 15.4%, while the solution-processed equivalent only gave PCE of 8.6%. However, in one-step co-deposition it is

difficult to simultaneously control the deposition rates of both precursors, potentially leading to undesirable non-stoichiometric film. A sequential vapor deposition method can be applied, as shown by Hu *et al.*[37] A bilayer film is first prepared from sequential deposition of PbI_2 and CH_3NH_3I, both of which should partially react *in situ* during the vacuum-deposition of CH_3NH_3I, followed by post-deposition thermal annealing to complete the perovskite conversion process as well as to enhance film texturing. The smooth polycrystalline perovkite film with grain size of ~ 500 nm demonstrated an efficiency of 5.4% when used in device with a simple architecture with no interlayers (ITO/CH_3NH_3I/C_{60}/Ag). Chen *et al.* implemented *in situ* heating during the vapor deposition of CH_3NH_3I to improve perovskite conversion and crystallization, resulting in ITO/PEDOT:PSS/$CH_3NH_3PbI_{3-x}Cl_x$/C_{60}/Bphen/Ca/Ag device with PCE of 15.4%.[38]

Chen *et al.* presented a "hybrid" approach between both solution- and vacuum-based approaches by using vapor-assisted solution process (VASP).[39] Planar devices prepared from this approach demonstrate promising efficiency of 12.1%. The PbI_2 film is first deposited by spincoating, followed by the exposure in a CH_3NH_3I-vapor-rich environment under elevated temperature. The CH_3NH_3I vapor is generated by heating the precursor powder in a closed container. Akin to the other two-step approaches discussed before, VASP takes the advantage of a more kinetically controlled CH_3NH_3I diffusion into PbI_2 framework to generate a more thermodynamically stable compact perovskite film with well-defined grains.

In brief, two-step deposition method (whether solution-based or vacuum-based or combination of both), despite it intricacy, allows for independent control in the deposition conditions of each precursors and hence their reaction thereafter. This eventually enables a better control over the perovskite film formation process.

2.2 Solvent engineering

Solvent engineering approach demonstrated by Jeon *et al.* is an attractive approach to circumvent the limitations of one-step spincoating process, which tends to yield inhomogeneous perovskite films hampering its reproducibility.[29] Perovskite film is deposited from a precursor solution dissolved in a mixture of dimethylsulfoxide (DMSO) and γ-butyrolactone (GBL) (DSMO:GBL = 3:7 v/v), immediately followed by a toluene drip while the substrate is spinning (Fig. 2). DMSO is used due to its strong coordination with PbI_2 to form lead halide-solvent complex, while GBL with higher boiling point behaves purely as a solvent. Mixed-solvent approach alone has also been shown by Kim *et al*., who used a combination of *N,N*-dimethylformamide (DMF) and GBL (DMF:GBL = 97:3 v/v), to prepare perovskite film with improved morphology.[40] Toluene is chosen due to its miscibility with both DMSO and GBL yet it does not dissolve the precursor materials. The toluene drip, therefore, removes excess DMSO solvent and this encourages supersaturation in the cast film and hence fast nucleation. PbI_2-DMSO impedes the rapid reaction between perovskite precursors, leaving a highly uniform CH_3NH_3I-PbI_2-DMSO complex film. This complex film can be converted into crystalline perovskite when DMSO escapes from the film during annealing. These intermediate complex species essentially moderate the rate of formation of the final perovskite. Planar device with the configuration of FTO/TiO_2/$CH_3NH_3Pb(I_{1-x}Br_x)_3$/PTAA/Au exhibited a PCE of 9.1% under forward scan (short-circuit to open-circuit) and 14.4% under reverse scan (open-circuit to short-circuit), which indicates a large hysteresis. By contrast, the corresponding mesoscopic mixed halide perovsktie device prepared on a 200-nm-thick mesoporous TiO_2 scaffold showed PCE of 15.8% and 15.9%, for forward and reverse scans, respectively.

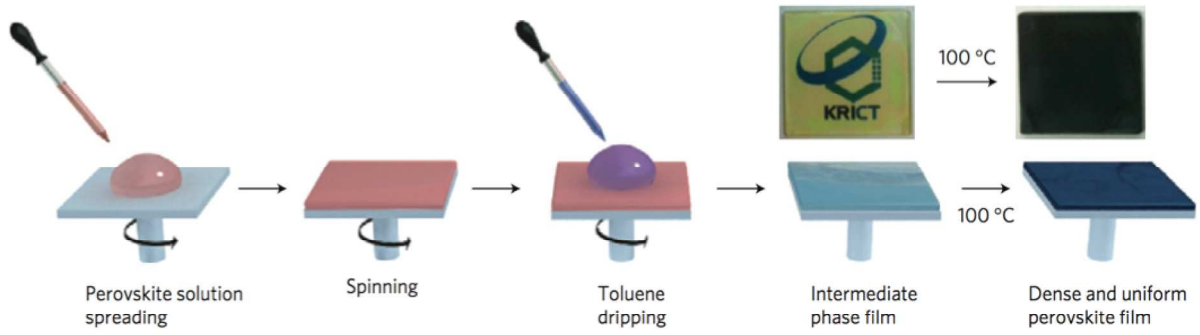

Fig. 2 Schematics of solvent engineering procedure to prepare perovskite thin film.[29]

Reporting independently, Wu *et al.* showed that the use of DMSO solvent itself was sufficient to yield highly uniform PbI_2 films, which were sequentially immersed into the organohalide solution to convert to perovskite.[41] Indeed, the use of DMSO could simultaneously solve two main issues associated with sequential deposition technique: (1) incomplete conversion of thick PbI_2 film to CH_3NH_3I especially in the absence of mesoporous scaffold, and (2) inconsistent degree of conversion resulting in polydispersed crystal size. Both issues originate from the lack of control in PbI_2 crystallization leading to varying crystal sizes and poor film uniformity. Since it is a diffusion-limited process, the conversion is largely dependent on CH_3NH_3I penetration into PbI_2 film. By using a more strongly coordinating solvent such as dimethylsulfoxide (DMSO), they were able to manipulate the rate of PbI_2 crystallization *via* formation of $PbI_2(DMSO)_2$ complexes. The sequentially deposited CH_3NH_3I film exhibited a smoother surface with smaller crystals compared to the film prepared with DMF, a more weakly coordinating solvent with Pb^{2+}. Consequently, this improvement in the control of the crystallization process is translated to higher reproducibility in the fabrication of DMSO-based perovskite devices.

2.3 Rapid solvent removal

The unconstrained crystallization of perovskite during deposition can be attributed to a certain extent to the slow solvent evaporation rate, which in turn dependent on its boiling point and the spincoating conditions. Huang *et al.* introduced an additional step of flowing Ar gas over a semi-wet perovskite film during spincoating process to accelerate solvent drying.[24] This gas-assisted step induces supersaturation that results in the formation of a large number of nuclei in the perovskite solution. Post-deposition annealing further promotes the crystal growth, yielding films with densely packed single crystalline grains. The planar device constructed with this approach gave PCE of up to 14% with good reproducibility, while the conventionally spin-coated film resulted in a much lower PCE of 4.6%.

Other than using gas-assisted drying, rapid solvent removal can also be achieved by using a non-dissolving solvent such as chlorobenzene (CB). This solvent has to have good miscibility with the host solvent but poor solubility for the perovskite precursors. Xiao *et al.* implemented such one-step, solvent-based method to achieve highly uniform $CH_3NH_3PbI_3$ films.[20] The planar devices prepared with this approach gave high PCE of 13.9%. The CB drip removes any excess DMF and rapidly reduces the precursor solubility, resulting in supersaturation condition very rapidly and this drives crystals nucleation and growth process. This approach greatly resembles the solvent method (DMSO/GBL/toluene) developed by Jeon *et al*.[29] Despite the similar protocols, the presence of DMSO that coordinates strongly with lead halide and this prevents immediate crystallization upon toluene drip, as observed from the lack of color change in the film. On the other hand, CB drip instantly promotes darkening, which suggests instantaneous perovskite formation. In both cases, good film quality and hence good device performance can be achieved and this may suggest that the coordinating solvent is less critical for uniform films

when fast nucleation have taken place. By controlling the degree of supersaturation in the deposited perovskite solution, either using gas-assisted or solvent-assisted approach, it is possible to have a better control over the crystallization process during the film formation.

2.4 Chloride introduction

Unlike their mesoscopic counterparts, planar perovskite devices, based on organolead mixed halide $CH_3NH_3PbI_{3-x}Cl_x$ have enjoyed more success compared to the pure triiodide system.[5] One possible reason to explain this observation is the modulation of crystallization with the presence of chloride ions and this has a more significant effect on the planar system than a mesoscopic system. Hence the doping with chloride ions, from either metal chloride (*e.g.*, $PbCl_2$) or organochloride (CH_3NH_3Cl), is another effective method to improve the morphology of perovskite films.[7,42] The modified morphology in the mixed halide perovskite may be the reason for its much longer electron-hole diffusion length, exceeding 1 μm, and roughly 10 times higher than that its triiodide counterpart.[13] Mixed halide perovskite film is typically prepared with a precursor ($PbCl_2$:CH_3NH_3I) ratio of 1:3. Post-deposition heat treatment induces chloride loss in the form of gaseous CH_3NH_3Cl with higher volatility than CH_3NH_3I, resulting in the formation of $CH_3NH_3PbI_3$. Therefore, these Cl^- ions can facilitate the removal of excess $CH_3NH_3^+$ ions even at low annealing temperatures.[43] It has been reported that there is only a negligible amount of chloride phase in the final perovskite film. In addition, the characteristic X-ray diffraction (XRD) peaks of the Cl-doped $CH_3NH_3PbI_3$ are identical to those without doping.[43-45]

Zhao and Zhu demonstrated the preparation of $CH_3NH_3PbI_3$ perovskite thin films by incorporating CH_3NH_3Cl into a typical precursor mixture of PbI_2 and CH_3NH_3I.[42] The presence of CH_3NH_3Cl altered the kinetics of the crystallization process (formation of $PbCl_2$),

significantly improved the perovskite film morphology as observed from the disappearance of sub-micron "islands". The mixed halide film also had improved optical absorption. As a result, the planar devices exhibited an improved PCE from 2% to 12% upon CH_3NH_3Cl incorporation. Chloride ions can also be introduced by immersing PbI_2 film into a mixed solution of CH_3NH_3I and CH_3NH_3Cl.[23] The chloride doping results in: (1) smooth morphology with distinct crystals; (2) enhanced lifetime of the photoexcited species; (3) improved light absorption, and (4) decreased series resistance of the solar cell device; all of which contribute to a high PCE of 15%. Inorganic salt such as NH_4Cl could also be employed as chloride source for organolead iodide perovskite, as shown by Zuo and Ding.[46] In comparison to CH_3NH_3Cl, NH_4Cl resulted in smoother films with better crystallinity and improved optical absorption. The inverted planar devices based on ITO/PEDOT:PSS/$CH_3NH_3PbI_3$/$PC_{61}BM$/Al showed a much higher PCE of 9.9% with NH_4Cl additive, as compared to 8.1% (with CH_3NH_3Cl additive) and 0.1% (without any additive).

The transient presence of chloride prompts the formation of chloride-iodide intermediate phase that alters the crystallization kinetics. These intermediate species possess distinct crystalline features that can be observed at the early stages of thermal annealing by looking at the x-ray diffraction patterns.[47] In the attempt to explain the possible origin of the intermediate mixed halide phase, Tidhar *et al.* hypothesized that in the mixture of $PbCl_2$ and CH_3NH_3I, $PbCl_2$ particles could act as heterogeneous nucleation sites for the formation of perovskites.[48] We believe this conjecture can be extended to the other chloride-doped systems owing to the possibility of ionic exchange between the different halide sources in solution. Nevertheless, Williams *et al.* demonstrated that there were subtle variations in the kinetics of the complex ion formation and aggregation in the solution depending on how the chloride is introduced.[49] The

chemical equilibria in the precursor solution, or the lack thereof, might affect the crystallite formation and transformation in the cast film. They further proposed that the chloride-rich intermediate species acted as templates facilitating topotactic self-assembly of the precursor materials into perovskite crystallites, which undermines the effect of substrate interfacial energy predominantly observed in pure iodide systems, before being lost *via* sublimation or degradation in the form of organochloride compounds during annealing process (Fig. 3).

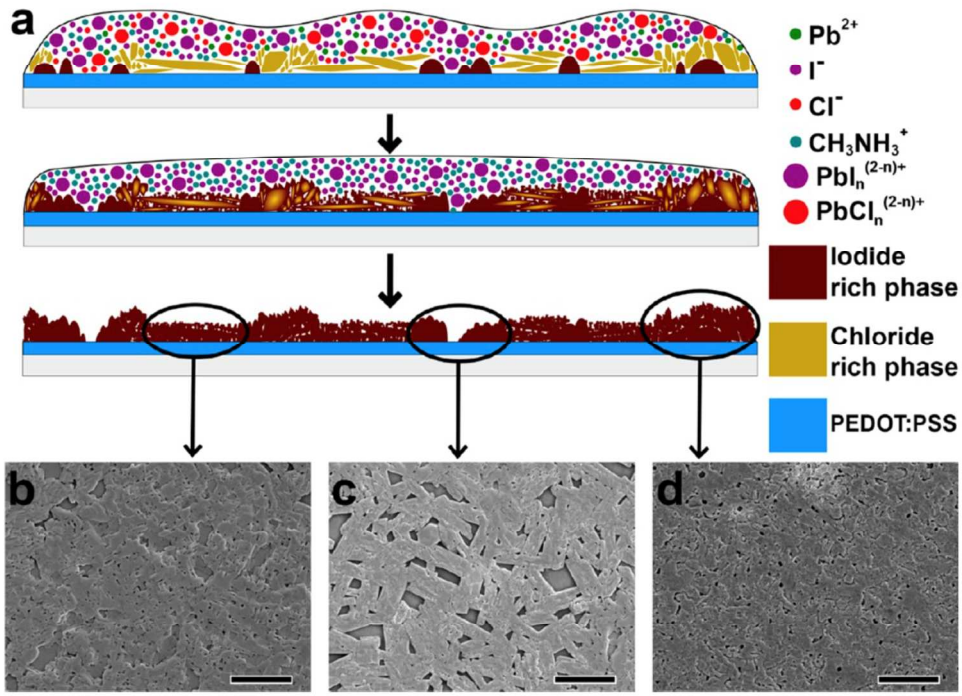

Fig. 3 (a) Schematics of morphological evolution in the $CH_3NH_3PbI_{3-x}Cl_x$ film: nucleation during precursor solution deposition (top), phase evolution and growth during annealing (middle), and final morphology (bottom), (b-d) Representative images of regions with different morphological constituents in the $CH_3NH_3PbI_{3-x}Cl_x$ film; the scale bars are 5 μm.[49]

The versatility of chloride incorporation can also be extended to mixed iodide-bromide organolead perovskites.[44,45] An evolution in morphology from one-dimensional (1D)-like

crystals (*e.g.*, fibers or nanobelts) into a more uniform crystalline film has been observed upon Cl^- inclusion. Similar to the pure iodide system, the chloride entities are proposed to promote the formation of ternary intermediate species comprising all the halide precursors, which subsequently alter the kinetics of perovskite transformation.

Although chloride ions have been known to have profound effect on perovskite morphology, their other functions as well as the verification of their perpetual existence in thin film remain disputable. There are, however, a few phenomena that can be explained by assuming actual presence of the chlorides. By performing density functional calculations, Du demonstrated that the high carrier diffusion length in the mixed chloride-iodide film was attributed to the significant increase in the formation energy of the interstitial defects, in turn caused by the reduced lattice constant due to the smaller Cl atoms.[50] On the other hand, Mosconi *et al.* discovered by first principle electronic structure calculations that interfacial Cl atoms at TiO_2 interface might lead to a stronger electronic coupling between mixed-halide perovskite and TiO_2, enhancing electron extraction between both materials.[51]

2.5 Precursor composition

Wang *et al.* observed a strong dependence of $CH_3NH_3PbI_3$ morphology on the stoichiometry ratio of its corresponding precursors.[52] Deposited under the same conditions with low-temperature solution processing on flat PEDOT:PSS-coated substrates, the equimolar solution (PbI_2:CH_3NH_3I = 1:1) demonstrates a rough morphology with microfiber formation. Reducing PbI_2 content in the precursor solution, *i.e.*, decreasing the precursor ratio, was observed to reduce the formation of the microfibers, gradually followed by the formation of a more compact film with fewer pinholes. Furthermore, it was also found that the precursor compositions in the

spincoated films were different from that in the solutions, which could be due to the varying interaction strength between the precursors and the substrate. The optimum precursor ratio was also found to be different for films with different thicknesses.

Another study on precursor composition was performed by Yu *et al.* on both mixed halide (I/Cl) and pure iodide perovskites.[43] Similar trend in the morphological evolution was observed with the reduction of PbI_2/CH_3NH_3I precursor ratio. It was, however, hypothesized that the organohalide-rich environment in films with low precursor ratios might have introduced certain intermediate phases, resulting in a retarded crystallization rate.

2.6 Solvent additive

Crystallization rate of perovskite can be also manipulated by incorporating additive molecules into the precursor solution. Two important criteria to consider in the selection of solvent additive are: (1) higher boiling point than that of the host solvent, and (2) preferential interaction with the precursor materials. One strategy to modulate the interaction with precursors is by taking the advantage of the chelating properties of molecules such as bidentate halides to metal ions such as Pb^{2+}. It is therefore possible to alter the crystallization kinetics and hence morphology of perovskite. Liang *et al.* employed 1,8-diodooctane (DIO) due to its high likelihood to coordinate with Pb^{2+} (from $PbCl_2$) during crystal growth as well as its higher boiling point (T_b = 332 °C) as compared to the host solvent DMF (T_b = 153 °C).[32] As a result, the interaction between DIO and Pb^{2+} becomes more prominent as most of the host solvent is removed during spincoating. The chelation of DIO with $PbCl_2$ might have induced the formation of a more thermodynamically stable intermediate structure, which leads to the modification of crystallization rate. The DIO-treated film exhibits smooth morphology with improved surface coverage.

2.7 Thermal annealing and "flash" annealing

Heat treatment performed on perovskite films typically serves a few purposes: (1) to remove residual solvent from solution processing; (2) to assist perovskite formation from its precursors, and (3) to enhance crystallization and grain growth. Depending on the conditions employed during thermal annealing process (*e.g.*, temperature, duration, ambient atmosphere) as well as the attributes of the perovskite films exposed to the heat treatment (*e.g.*, film thickness, film composition), distinct morphologies could be obtained. A mixed halide perovskite typically has to be annealed longer to achieve full conversion compared to the single halide system. Hybrid perovskite films that survive thermal annealing can be considered to be more thermally stable at room temperature. Eperon *et al.* were able to optimize the morphology of $CH_3NH_3PbI_{3-x}Cl_x$ perovskite film deposited on planar substrates by fine-tuning the thermal annealing conditions.[28] Both prolonged heat treatment and annealing at higher temperature typically caused coarsening of the perovskite crystals with decrease in surface coverage while the use of thicker films improved surface coverage upon annealing. Based on these results, it may be sensible to use thick $CH_3NH_3PbI_{3-x}Cl_x$ film and anneal it at lower temperatures to improve surface coverage. Dualeh *et al.* found out that a minimum temperature of 80 °C was required to convert $PbCl_2$ and CH_3NH_3I mixture into $CH_3NH_3PbI_3$ perovskite.[53] Similar to the observation obtained by Eperon *et al.*, annealing at higher temperatures induced the "island" formation, which was accompanied by increased content of PbI_2 phase *via* CH_3NH_3I loss, resulting in decrease in device performance.

The conventional thermal annealing treatment of perovskite can be coupled with "flash" annealing, *i.e.*, rapid ramping to a higher temperature followed by brief heating; the latter step

modifies the perovskite morphology.[54,55] Saliba *et al.* showed that "flash" annealing was more effective for planar architecture, while the mesoscopic device suffered from reduced surface coverage.[54] Therefore, it is crucial to consider the different types of device configuration when devising heat-treatment methodologies. Expectedly, "flash" annealed planar device demonstrated an improved efficiency.

2.8 Solvent annealing

Solvent annealing has been demonstrated as an attractive strategy to optimize the morphology of organic solar cells.[56] Essentially, a semiconductor film is placed in an environment saturated with solvent vapor. The first demonstration of solvent annealing for organolead perovskite film was given by Xiao *et al*., who annealed the $CH_3NH_3PbI_3$ in the presence of DMF vapor.[25] By employing solvent annealing, the perovskite crystals can grow more extensively because the DMF vapor, in which both PbI_2 and CH_3NH_3I precursors are highly soluble, can facilitate the diffusion and reorganization of the precursor molecules and ions. Interestingly, it was also found that the crystal growth was dependent on the film thickness, *i.e*., thicker films (more materials present) could produce larger grains as high as 1 μm (Fig. 4). The inverted planar devices prepared with solvent-annealed $CH_3NH_3PbI_3$ did not exhibit a strong dependency of device performance on film thickness. Even the thickest perovskite film prepared (1 μm thick) was able to yield PCE approaching 15%, which was comparable to those of the thinner films.

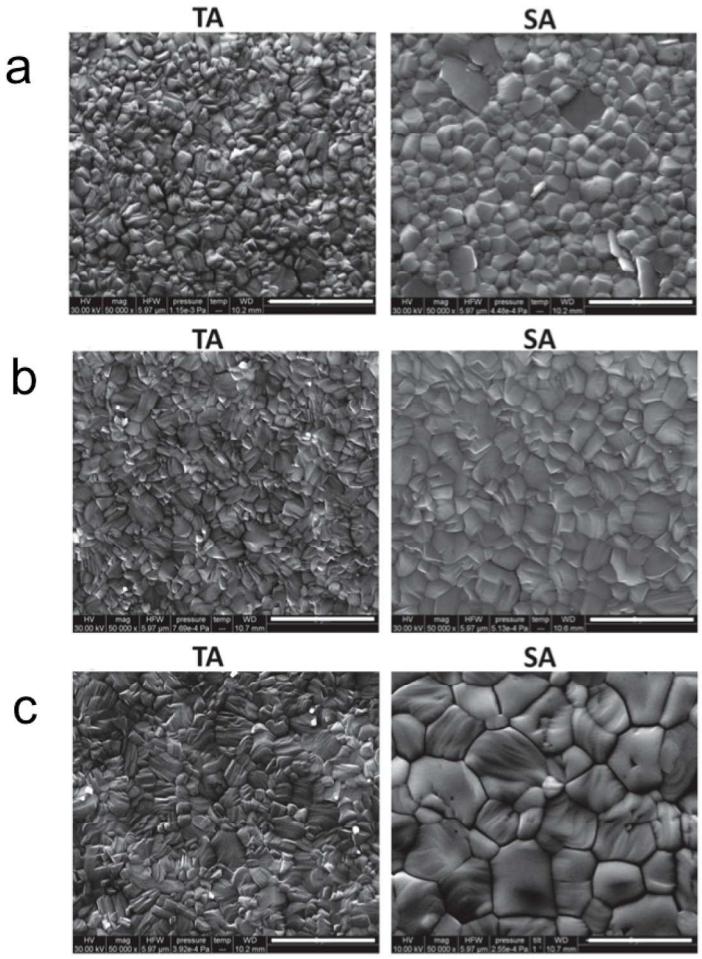

Fig. 4 SEM images of the thermally-annealed (TA) and solvent-annealed (SA) perovskite films with thicknesses of (a) 250 nm, (b) 430 nm and (c) 1015 nm; the scale bars in the SEM micrographs are 2 *μ*m.[56]

2.9 Humidity effect

Ambient conditions, such as the amount of solvent vapor or humidity, may influence the crystallization of hybrid perovskite. In particular, humidity is an important factor to consider due to the ease of organometal halide perovskite to degrade in highly humid environment. Zhou *et al*. demonstrated that the mixed halide $CH_3NH_3PbI_{3-x}Cl_x$ perovskite underwent different conversion

process when annealed under controlled humidity (30% RH).[5] Strong $CH_3NH_3PbCl_3$ phase could be observed in the film annealed with moisture involvement, which could otherwise not be found in the dry air conditions. The presence of small amount of moisture alters the transformation route by partially dissolving the reacting entities and enhancing mass transport in the film. This so-called "enhanced reconstruction" strategy resulted in improved PCE from 13.5% to 16.4% for TiO_2/perovskite/spiro-OMeTAD device. The same strategy has also been successfully applied in solar cell with different architecture (PEDOT:PSS/perovskite/$PC_{61}BM$), boosting PCE from 12.3% to 15.4%.[57]

Perovskite film with excellent uniformity and large crystal size can be obtained through careful control of the nucleation and growth process. Based on the discussion so far, the general conclusion is that nucleation should be encouraged for the formation of films with good uniformity and thereafter, growth should be controlled. Nucleation can be encouraged by either achieving the supersaturation conditions quickly through rapid solvent removal or through the fast formation of some intermediate nuclei. Crystallization of the films can be promoted using post-deposition annealing techniques to obtain crystals of optimal size.

3. Device architecture

Device performance of perovskite solar cells are highly dependent on its architecture which will in turn dictate the choice of materials, the deposition methods for the material and naturally, the compatibility between the different components in the device. Two major embodiments of perovskite solar cells have been developed so far, *i.e.*, mesoscopic and planar structures. In the mesoscopic architecture, the perovskite can either be introduced as a thin layer that will just adequately cover the oxide scaffold with the pores in the scaffold infiltrated with charge

transporting material (Fig. 5a), or the perovskite can form an overlayer on top of the completely infiltrated oxide scaffold (Fig. 5b). A more straightforward planar architecture can exist in either conventional (Fig. 5c) or inverted (Fig. 5d) configuration, depending on the direction of electric current.

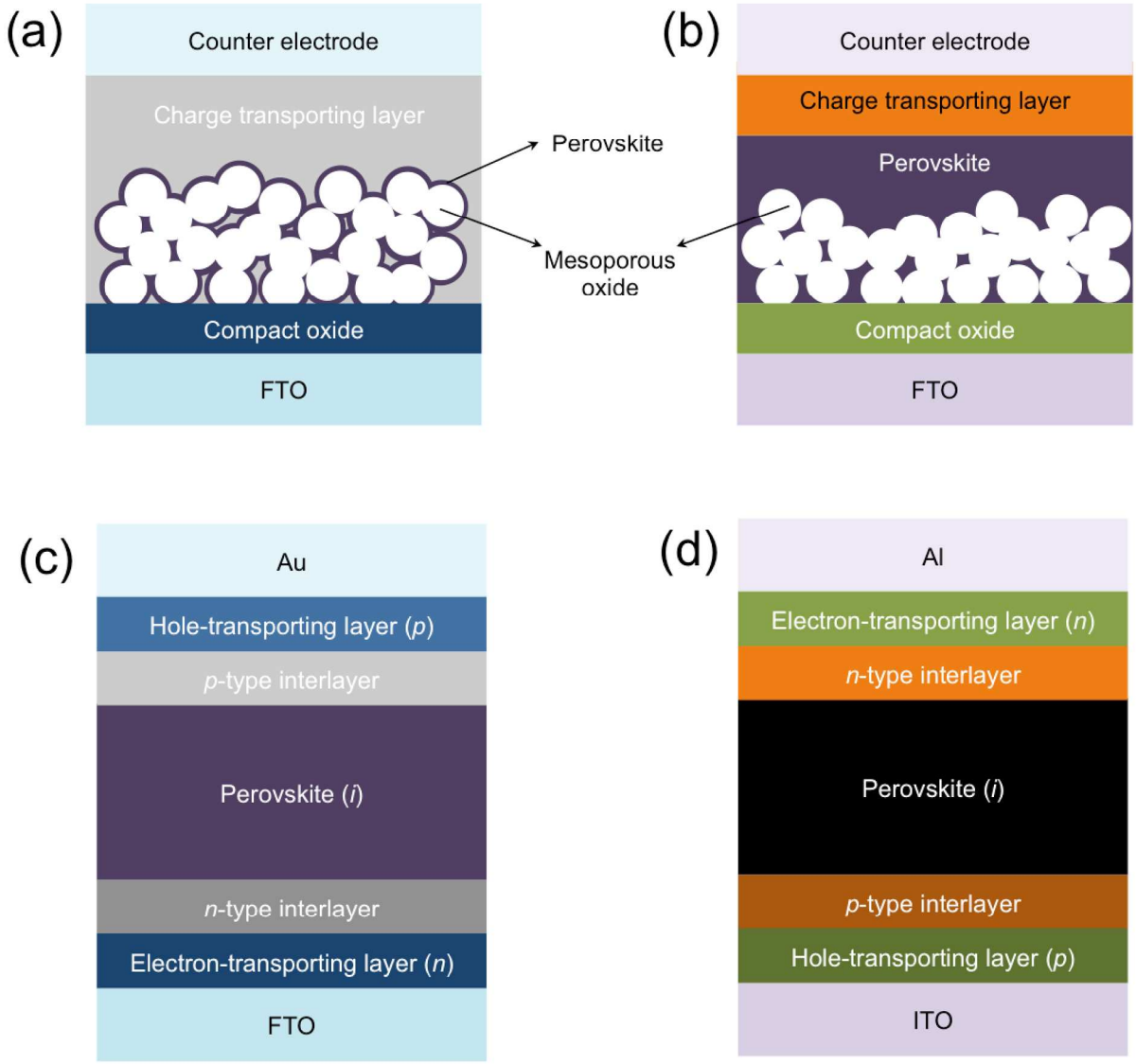

Fig. 5 Schematic diagram of mesoscopic heterojunction solar cells (a) no perovskite overlayer, (b) with perovskite overlayer; and planar heterojunction solar cells with (c) conventional "*n-i-p*" and (d) inverted "*p-i-n*" configurations.

3.1 Mesoscopic architecture

Since the initial evolution of perovskite solar cells was founded on a mesoporous (mp) structure, there are already several review papers on mesoscopic perovskite solar cells.[58-67] Thus, in this section, we will only focus our discussions on metal oxide scaffolds and hole-transporting materials (HTMs) for mesoscopic perovskite solar cells to avoid repetition of the existing accounts of this type of solar cell. As presented earlier in the introduction section, by considering the functions of the metal oxide scaffold, all the mesoscopic perovskite solar cells demonstrated so far can be classified into the following two groups.

3.1.1 Mesoscopic perovskite solar cells with active scaffolds

Of the active scaffolds for mesoscopic perovskite solar cells studied so far, TiO_2 nanoparticles have been the most commonly employed materials. It is still under debate whether the presence of a scaffold is a prerequisite to obtain perovsksite solar cells with enhanced device performance. However, many publications suggest that the efficiency of mesoscopic perovskite solar cells is strongly related to the thickness of the TiO_2 scaffold layer. By investigating $CH_3NH_3PbI_3$ solar cells with mp-TiO_2 layer ranging from 0.6 μm to 1.5 μm, Kim *et al.* found that quite unlike solid state DSSCs which required a thick TiO_2 scaffold (~ 3 μm) to achieve sufficient absorption, hybrid lead iodide perovskite sensitized solar cells only need a submicron thick mesoporous TiO_2 layer to achieve good performance.[8] The best performance of over 9% was from the device with at least 600-nm-thick mp-TiO_2 layer. Leijitens *et al.* attributed the dependence of the device performance on the thin layer of mesoporous TiO_2 layer to a perovskite pore filling effect (Fig. 6).[68] They found that the pore filling fractions were heavily dependent on the TiO_2 scaffold thickness. When certain concentrations of perovskite precursor solutions were used for

deposition, there was always an accompanying required thickness of mp-TiO_2 layer so that perovskite could form continuous films onto the mesoporous TiO_2 rather than discrete small nanoparticles. In general, a perovskite precursor solution with higher concentration can only completely fill the pores in a thinner mp-TiO_2 film. Based on their calculations, for high concentration of perovskite precursor solution (40 wt%), a thin mp-TiO_2 (~ 300 nm) is needed to ensure high device performance. A completely perovskite-filled TiO_2 architecture can lead to high device performance because there will be high electron density in the TiO_2, improving the charge transport rates and collection efficiency. In addition, the recombination between TiO_2 and HTM could be minimized by the presence of perovskite over all the TiO_2 surfaces.

Estimation of Perovskite Pore Filling and Coating Thickness

meso-TiO_2 thickness	750 nm	750 nm	440 nm	260 nm
perovskite concentration	30 wt %	40 wt %	40 wt %	40 wt %
pore filling fraction (%)	47 ± 2	70 ± 3	108 ± 4	100 ± 5

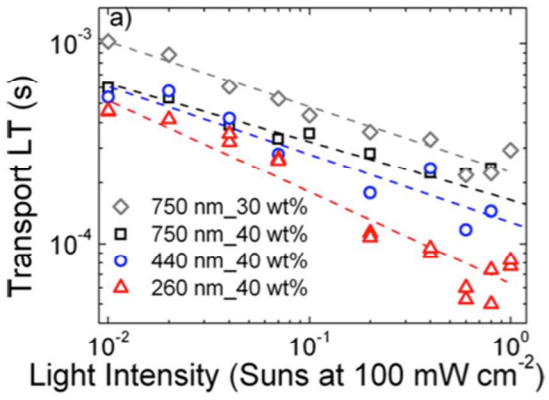

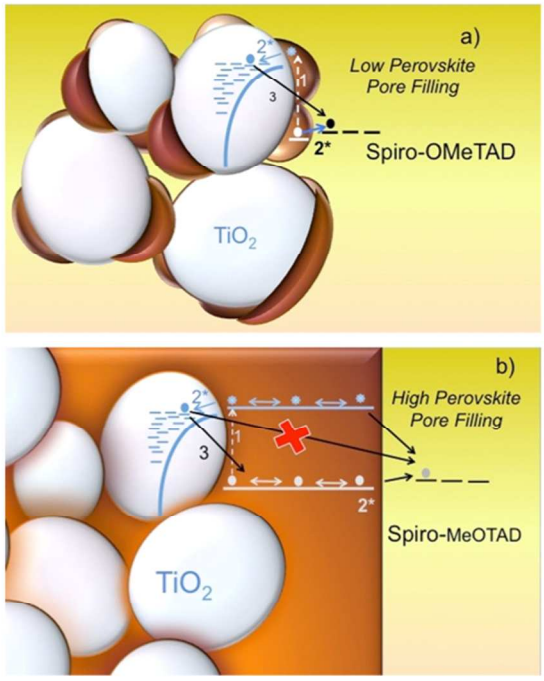

Fig. 6 The transport lifetimes of devices with various pore filling fraction as a function of light intensity obtained from small perturbation photocurrent decays, and the proposed recombination mechanism for solar cells with incomplete and complete perovskite pore filling.[68]

It should be noted that besides TiO_2 nanoparticles, TiO_2 nanocrystals in other shapes (*e.g.*, nanorods, nanowires, nanofibers, nanotubes and nanocones) and similar *n*-type materials such as ZnO have been applied to make the scaffold for mesoscopic perovskite solar cells, which can also act as efficient electron collector.[69-75] In particular, solar cells employing single-crystalline rutile TiO_2 nanocones were observed to outperform the nanorod-based devices due to a more efficient electron transfer from perovskite to TiO_2.[75] Furthermore, active scaffold materials are not only limited to *n*-type semiconductors. Tian *et al.* first demonstrated a new type of efficient mesoscopic perovskite solar cells based on the mesoporous *p*-type metal oxide NiO.[76] It was found that the FTO/NiO_x/mp-NiO/$CH_3NH_3PbI_3$/$PC_{61}BM$/BCP/Al device (where $PC_{61}BM$ – phenyl-C_{61}-butyric acid metyl ester) could achieve a PCE of 1.5%. Recently, Wang *et al.* obtained a more impressive PCE of 9.51% with similar device architecture (ITO/NiO_x/mp-NiO/$CH_3NH_3PbI_3$/$PC_{61}BM$/BCP/Al, where BCP – bathocuproine).[77] Transient absorption and photoluminescence studies confirmed that efficient charge transfer occurred at the NiO/perovskite heterojunction. They further improved the efficiency of the device PCE to 11.6% by employing a low-temperature sputtered NiO_x compact film, instead of a solution-processed one.[78] The use of a *p*-type mesoporous layer for hole transport and collection shown in these studies increases the diversity of perovskite solar cells, and this is also a good way to remove the unstable hole-conducting organic materials often used in mesoscopic perovskite solar cells.

Active scaffolds can also be decorated with quantum dots (QDs) such as lead sulfide (PbS) to achieve co-sensitization with organolead halide perovskite that leads to a panchromatic response from the visible to the near-infrared (NIR) region.[79] Quantum dots not only improve the photon harvesting, but they can also assist charge transport from perovskite to TiO_2. Besides semiconducting QDs, C_{60}-SAM, graphene and its composites have also been applied as

interfacial layer to improve charge transfer between perovskite and the active scaffold.[80-82] The use of TiO_2-graphene composite, for instance, resulted in a low-temperature processed electron collection layer with perovskite solar cell demonstrating remarkable efficiency of 15.6%. Therefore, material selection and combination in systems employing active scaffolds are important considerations to obtain highly efficient solar cells.

3.1.2 Mesoscopic perovskite solar cells with passive scaffolds

One of the main advantages of mesoscopic perovskite solar cells with passive scaffold is their low-temperature solution processability. When an Al_2O_3 passive scaffold was used in perovskite solar cells, it required high temperature (500 °C) sintering to remove the organic binders inside the thin film, very similar to the preparation of mesoporous TiO_2. Later, Ball *et al*. introduced a low-temperature approach to prepare an Al_2O_3 mesostructured scaffold *via* solution deposition of Al_2O_3 nanoparticles without any binder, which were subsequently sintered at 150 °C to form the Al_2O_3 film.[11] They demonstrated that the $CH_3NH_3PbI_{3-x}Cl_x$ perovskite solar cells prepared on the low-temperature-processed Al_2O_3 scaffold could achieve PCE up to 12.3%, with V_{OC} of 1.02 V, J_{SC} of 18 mA/cm^2, and FF of 0.67. It was also the first time that the multifunctional roles of perovskite (light absorption, charge generation, ambipolar electron and hole transport) in solar cells were clearly shown, which was partially responsible for leading to the development of scaffold-less planar perovskite solar cells. In the subsequent work, Wojciechowski *et al.* demonstrated that it is possible for all the layers in these mesoscopic perovskite solar cells to be processed at low-temperature by reducing the processing temperature for highly crystalline TiO_2 compact layer to less than 150 °C.[83] The optimized device showed a maximum PCE of 15.9%. This renders mesoscopic perovskite solar cells to be even more cost-competitive and compatible

with flexible substrates. It should be mentioned that besides Al_2O_3, insulating ZrO_2 nanoparticles have also been employed to construct the mesoporous layer for $CH_3NH_3PbI_3$ and the resulting solar cells could give a PCE of 10.8%.[84] Hwang *et al.* demonstrated the use of SiO_2 nanoparticles as a scaffold layer. By employing nanoparticles with an optimum size of about 50 nm, they can obtain better perovskite infiltration and hence achieve a PCE of 11.5% with V_{OC} of 1.05 V, which was higher than those of the TiO_2 nanoparticles devices.[85]

Similarly, the effect of the thickness of the passive scaffold on the device performance of mesocopic perovskite solar cells has been studied. Ball *et al.* have demonstrated that J_{sc} of FTO/bl-TiO_2/mp-Al_2O_3/$CH_3NH_3PbI_{3-x}Cl_x$/HTM/Ag (where bl-TiO_2 refers to the TiO_2 blocking layer) can be tuned by varying the thickness of mesoporous Al_2O_3 layer (Fig. 7).[11] J_{SC} of these perovskite solar cells increased slowly with the reduction in Al_2O_3 thickness, reaching a maximum at the thickness of 80 nm (16.9 mA/cm^2). The cross-section of these devices showed that a capping layer of perovskite formed on mesoporous Al_2O_3 layer when the scaffold thickness was less than 400 nm. The presence of Al_2O_3 scaffold can also act as buffer layer to impede current leakage between the electrodes. In a very recent study, Mei *et al.* did a detailed investigation on the role of perovskite capping layer in mesoscopic perovskite solar cells.[67] It was found that the improved photocurrent when the capping layer is present was to a large extent due to the thick perovskite layer present in the system which enhanced the light absorption and larger perovskite particles in the capping layer which enhanced the light scattering.

In terms of the working mechanism, Kim *et al.* concluded from their impedance spectroscopy measurements that perovskite solar cell on a passive scaffold (ZrO_2) behaved similarly to a thin-film solar cell, in which the light absorber also works simultaneously as ambipolar electron and hole transporters, in contrast to perovskite solar cell on an active scaffold (TiO_2) that behaved

halfway between a mesoscopic DSSC and a thin-film solar cell.[86] The other feature of mesoscopic perovskite solar cells fabricated with passive scaffold is the absence of photovoltage loss observed in their active-scaffold counterparts. As reported by Lee *et al.*, comparable perovskite devices with TiO_2 and Al_2O_3 scaffolds exhibited V_{OC} of 0.8 V and 0.98 V, respectively.[7] The difference in photovoltage is attributed to the variation in "chemical capacitance" of the oxide, which is essentially related to the charge-storing capacity caused by the presence of sub-band gap states. Insulating Al_2O_3, inherently lacking of surface and sub-band gap states, results in significant decrease in chemical capacitance of the solar cell. These states, which can also act as charge trapping sites, can influence the long-term stability of the device, which is discussed in section 4.

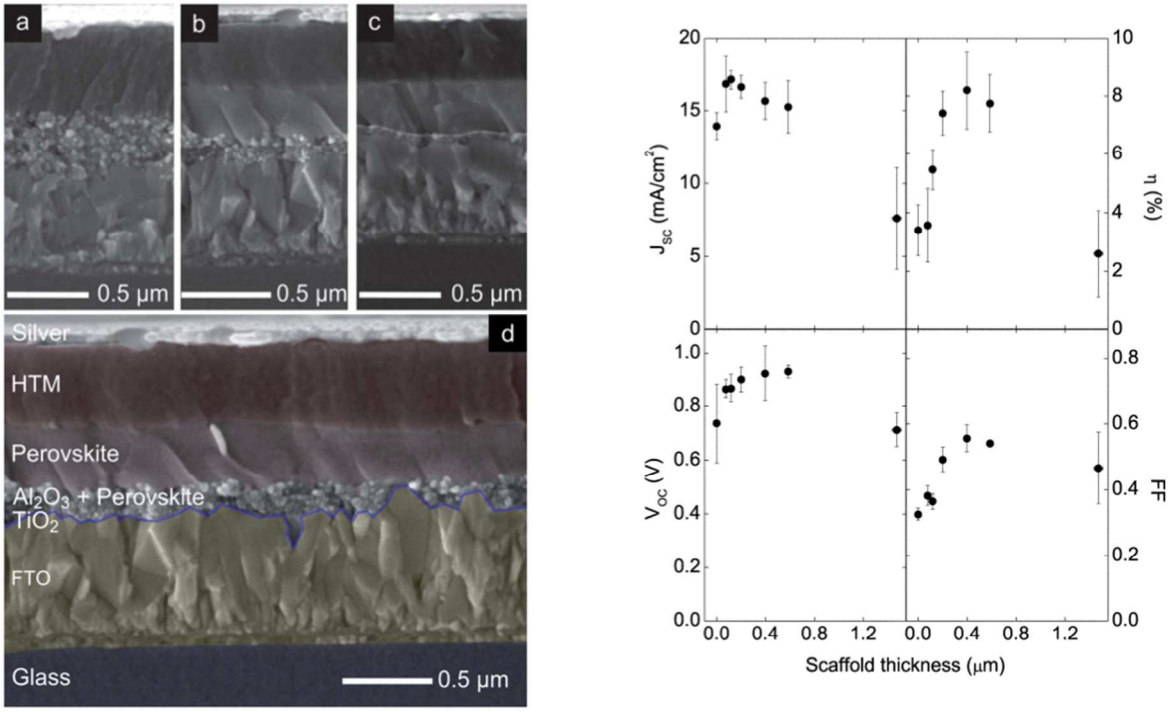

Fig. 7 Cross-sectional SEM images of FTO/bl-TiO_2/mp-Al_2O_3/perovskite/HTM/Ag solar cells with different thickness of Al_2O_3 scaffold, and the dependence of device parameters on the scaffold thickness.[11]

Recently, Edri *et al.* used the electron beam-induced current (EBIC) technique to study the working mechanism of $CH_3NH_3PbI_{3-x}Cl_x$ solar cells.[87] The appearance of two EBIC peaks at perovskite/electron acceptor (compact TiO_2 layer) and perovskite/hole acceptor (HTM) junctions regardless of the presence of the insulating mesoporous Al_2O_3 layer indicates that $CH_3NH_3PbI_{3-x}Cl_x$ solar cells have a *p-i-n* characteristic with an in-homogeneous built-in field, which is independent of the alumina scaffold. This is direct evidence that mesoporous Al_2O_3 layer in perovskite solar cells acts only as a scaffold. Besides, the higher photovoltage in mesoscopic perovskite solar cells with inert scaffold is believed to arise from the mutual contribution of both half junctions in series, each of which could minimize the dark current and maximize the photocurrent.

3.1.3 Hole transport materials (HTMs) for mesoscopic perovskite solar cells

As discussed earlier, spiro-OMeTAD is the most commonly used hole HTM for perovskite solar cells, mainly because it has been well studied as a HTM in OLEDs[88] and solid state DSSCs[64,89]. Solar cells based on hybrid lead halide coupled with spiro-OMeTAD as HTM have achieved PCE of more than 15%.[17,35] However, the cost of spiro-OMeTAD remains unfortunately high mainly because of its lengthy and low yielding synthesis. The limitation in HTM options has proved to be a major impediment to the growth and advancement of high efficiency, cost-effective perovskite solar cells. Hence it has become imperative to design and develop more economical alternative HTMs to spiro-OMeTAD. In view of this, much attention has been paid to the development of new HTMs in recent years. Mesoscopic perovskite solar cells have so far been used as the benchmark for many novel HTMs, and thus we summarize the progress in this part.

Similar to solid-state DSSC (ssDSSC), HTMs for perovskite solar cells should primarily meet the following requirements: (1) good hole mobility; (2) a compatible HOMO energy level relative to organolead halide perovskites for efficient hole transfer; (3) good solubility and film forming properties, and (4) low cost. However, in perovskite solar cells, HTM is not required to fill in the pores, which are already filled by the perovskite materials; hence eliminating the pore-filling issues commonly encountered in ssDSSC, which widens the choice of materials. Three categories of HTMs have been investigated in perovskite solar cells: inorganic, polymer and small molecular HTMs. The chemical structures of the HTMs recently used in perovskite solar cells and their corresponding HOMO levels are respectively in Fig. 8 and Fig. 9.

The progress in inorganic HTMs, however, has been slow mainly due to the limited choice of materials. Well known inorganic HTMs such as CuI (PCE = 6%)[90], NiO (PCE = 11.6%)[78] and CuSCN (PCE = 12.4%)[91] have been investigated in mesoscopic perovskite solar cells. Though potentially cost-effective and stable under ambient conditions, these HTMs have shown inferior performance characteristics as compared to their organic counterparts.

Several polymer HTMs including poly(triarylamine) (PTAA) and poly(3-hexylthiophene-2,5-diyl) (P3HT), which generally have better hole mobilities than small molecule HTMs and good film-forming properties, have been tested by Heo *et al*.; among them, PTAA demonstrated the highest efficiency of up to 12% compared to 6.7% for P3HT.[92] This was the first major breakthrough in the development of polymer HTMs, which suffered from pore-filling ability as reported for ssDSSC. Later the same group used a mixed-halide perovskite with PTAA and obtained a certified PCE of 16.2% (J_{SC} = 19.6 mA/cm^2, V_{OC} = 1.11 V and FF = 0.74); an even higher certified PCE of 17.9% has also been recently reported.[29,93] Chen *et al.* reported a P3HT/MWNTs (multi-walled carbon nanotubes) composite as HTM which showed higher PCE

(6.45%) than pristine P3HT (PCE = 4.1%).[94] MWNTs in a P3HT/MWNT composite act as efficient nanostructured charge transport tunnels and induce crystallization of P3HT, hence significantly enhancing the conductivity of the composite. The fill factor of the hybrid solar cells was greatly enhanced from 45% to 57%. Similarly, Habisreutinger *et al.* employed P3HT-functionalized single-walled carbon nanotubes (SWNTs) to substitute the traditionally used organic HTMs, showing a high PCE of up to 15.3% with an average efficiency of ~10%.[95] Xiao *et al.* reported that polyaniline (PANI), which acted as both sensitizer and HTM, gave a PCE of 7.34%[96]. The PCE only reduced slightly (from 7.3% to 6.7%) after 1000 hours, indicating the device has good long-term stability.

Unlike inorganic HTMs, organic-based HTMs have flexibility in tuning the oxidization potentials and the surface properties. One of their attractive features is that high V_{OC} can be achieved with the combination of $CH_3NH_3PbBr_3$ perovskite light absorber and HTMs with deeper HOMO levels. Early research has been done by Cai *et al.* using diketopyrrolopyrrole (DPP)-carbazole based polymer HTM (PCBTDPP).[97] The polymer HTM has a HOMO level of –5.4 eV and demonstrates a V_{OC} of 1.16 V. An even higher V_{OC} of 1.5 V was reported recently with 4,4'-bis(*N*-carbazolyl)-1,1'-biphenyl (CBP).[98] The $CH_3NH_3PbBr_3$ perovskite typically lacks light absorption in longer wavelength and is thus unfavorable to get a high efficiency. However a moderate PCE (6.7%) and a high voltage output (1.4 V) were achieved by Guo *et al.* with triarylamine-based polymer HTM (PIF8-TAA).[99] Another interesting feature of polymer HTMs was demonstrated by Kwon *et al.* with hydrophobic DPP based polymer (PDPPDBTE).[100] This polymer has a deep HOMO level of –5.4 eV with a good hole mobility of 10^{-3} $cm^2/V{\cdot}s$; hence, the device showed a better PCE of 9.2% than 7.6% for spiro-OMeTAD. The hydrophobicity of

PDPPDBTE, verified with water contact angle measurement, should contribute to the good device stability that will be presented in section 4.

As compared to the previous two types of HTMs, there are more small molecular HTMs reported so far because of the degree of freedom for designing. In designing small molecule HTMs, incorporating a triarylamine component seems to be essential. The nitrogen center acts as a doping site, which can be stabilized through conjugation with neighboring aromatic rings. The non-planar conformation of the triarylamine leads to longer intermolecular distances, which may result in a low hole mobility (10^{-5}–10^{-4} $cm^2/V{\cdot}s$), but in return, makes the molecules less crystalline and more suitable as a HTM.

Several groups have developed novel molecules in which triarylamine moieties were connected through an aromatic linker. Jeon *et al.* synthesized a few pyrene-core arylamine derivatives in which a pyrene core was substituted with various numbers of *N,N*-di-*p*-methoxyphenylamine moieties.[101] The best cells fabricated using these pyrene derivatives (Py-C) as a HTM showed a PCE of 12.4% under AM 1.5G illumination; one of the highest PCE values reported with small molecular HTMs other than spiro-OMeTAD, hence suggesting that very simple structures might still prove very useful as HTMs. Li *et al.* synthesized a new HTM, having ethylenedioxythiophene (EDOT) core substituted with triphenyl amine moieties (H101), yielding PCE of up to 13.8%.[102] The synthesis of this compound is much simpler and more efficient as compared to that of spiro-OMeTAD. Krishnamoorthy *et al.* reported a swivel-cruciform 3,3'-bithiophene-based HTM (KTM3) with a low lying highest occupied molecular orbital (HOMO) level.[103] This HTM, which exhibited varying performance depending on the *p*-type dopants used, demonstrated an optimized PCE of 11.3%. Krishna *et al.* synthesized novel amorphous HTMs based on a bulky triptycene core beneficial to prevent crystallization.[104] Triptycene core is

connected to diphenylamines *via* phenyl with/without thienyl groups and the device based on one of the derivatives (T103) showed PCE of 12.4%. Jeon *et al.* reported a PCE of 16.7% with a spiro-OMeTAD isomer with some of the methoxy substituents in the *ortho*- positions.[105] This is one of the highest PCEs reported for any novel small molecule HTM. Choi *et al.* have synthesized fused quinolizino acridine based-HTM (OMeTPA-FA) which produced a PCE of up to 13.6 %[106]. Do *et al.* synthesized star-shaped HTMs based on an electon-deficient triazine unit which showed PCE of up to 12.5%.[107]

Most of the abovementioned organic HTMs require additives such as Li salt, tBP or cobalt complex to improve their conductivity, hence enhancing the performance. Several groups have reported perovskite solar cells without incorporating additives into the HTM, which simplifies the fabrication procedures. Liu *et al.* reported tetrathiafulvalene derivative as HTM (TTF-1).[108] PCE of over 11% was obtained without the use of any dopants with this nitrogen-free HTM. In addition, lifetime of this cell under ambient conditions is 3 times higher than the cells with spiro-OMeTAD, possibly a result of this dopant free strategy. Qin *et al.* synthesized a donor-acceptor type quinolizino acridine-based HTM (fused-F) which showed PCE of up to 12.8%.[109] This HTM has a low bandgap and the LUMO level is close to that of the perovskite system, hence it serves both the function of light harvester, as well as hole conductor.

So far various approaches adopted by different groups in designing the HTM seem to give comparable results to those with the "standard" HTM (spiro-OMeTAD). Effective designing as well as optimizing thickness and additives is vital factor to get high efficiency. Future work needs to be done to study the HTM/perovskite interface,[110,111] which will shed some light on the underlying device physics and will help in the design of future molecules.

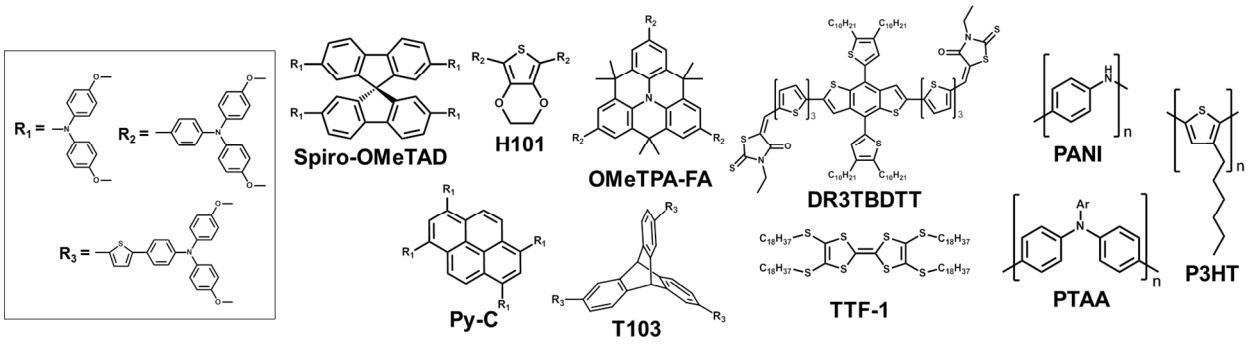

Fig. 8 Structures of some of the recently reported HTMs for perovskite solar cells.

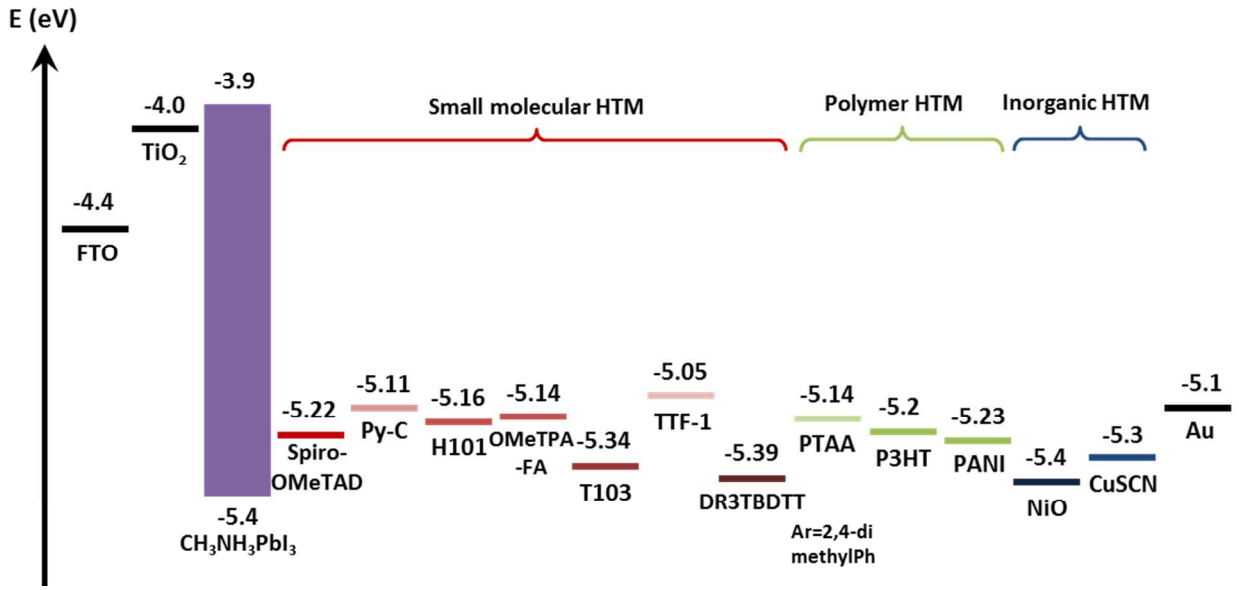

Fig. 9 Energy level diagram showing HOMO levels of various HTMs.

3.1.4 Hole-transporting material (HTM)-free mesoscopic perovskite solar cells

Although various novel HTMs have showed promising results, it is noteworthy to mention recent increasing attention towards HTM-free perovskite solar cells. Excellent semiconducting

properties (*i.e.*, long charge transport lifetime and ambipolar nature)[13,14] of organolead halide perovskite materials enable the elimination of hole transport layer; holes can be extracted by a suitable counter electrode. The simpler architecture in HTM-free devices leads to the reduction of the processing cost, which is advantageous for practical usage as they match with the low-cost solar cell applications and eliminate the air-sensitive spiro-OMeTAD. Etgar *et al.* demonstrated the initial study employing anatase TiO_2 nanosheets as the mesoporous layer.[112] The corresponding perovskite solar cell (FTO/c-TiO_2/mp-TiO_2/$CH_3NH_3PbI_3$/Au) displayed an efficiency of 5.5% (J_{SC} =16.1 mA/cm^2, V_{OC} = 0.63 V and FF = 0.57). It was revealed that in this type of solar cells, a depletion layer extends to both $CH_3NH_3PbI_3$ and TiO_2 films.[113] The build-in field of the depletion layer assists in the charge separation and suppresses the back reaction of electrons from the TiO_2 to the $CH_3NH_3PbI_3$ film. The device efficiency also strongly correlates with the width of the depletion layer, with the best performance achieved upon depletion of half of the TiO_2 film.[114] Further optimization of the quality of the perovskite layer resulted in efficiencies of 8–11%.[113-118]

Carbon electrode can be used to replace noble metal counter electrode (*e.g.*, Au or Ag) because of its earth abundance, large-scale printing processing, cost effectiveness and a more suitable work function of –5.0 eV (–5.1 eV for Au).[119-122] Mesoporous carbon electrode was screen-printed on a double layer of mp-TiO_2 and ZrO_2, followed by infiltration with perovskite through the carbon layer; PCE of 6.6% was achieved with device made with this electrode (FTO/c-TiO_2/mp-TiO_2/ZrO_2/$CH_3NH_3PbI_3$/C).[119] An improvement of PCE of up to 12.8% (J_{SC} = 22.8 mA/cm^2, V_{OC} = 0.86 V and FF = 0.66) was obtained by incorporating 5-ammoniumvaleric acid (5-AVA) to make a FTO/c-TiO_2/mp-TiO_2/ZrO_2/$(5\text{-AVA})_x(CH_3NH_3)_{1-x}PbI_3$ solar cell.[120] The 5-AVA cations act as the templates for the formation of the perovskite crystals on the mesoporous

scaffold, resulting in a more directed growth in the normal direction and better connected crystals; hence, lowering series resistance and increasing electrical conductivity. Even when unsealed, these HTM-free perovskite solar cells still demonstrate excellent ambient stability due to the protection imparted by the carbon electrode.

Various research works have clearly demonstrated that perovskite solar cells work as a *p-i-n* device and thus hole-transporting layer is no longer a prerequisite for device operation.[87,123] However, the device performance of HTM-free perovskite solar cells is still inferior to the state-of-the-art perovskite cells because of the poor efficiency of charge extraction and the charge recombination at interface; those cells typically show lower V_{OC} and FF. To improve charge extraction and to suppress the undesirable recombination, strategies such as controlling built-in field,[113,115] improving surface morphology,[116,117] and using insulating layer such as zirconium dioxide[119,120] have been demonstrated. This new device concept has greater potential for practical applications and further improvement in performance can be expected. A comparison of the resultant device performance with different HTMs, including HTM-free architecture is shown in Table 1.

Table 1 A few representative HTMs and their corresponding device performances.

Material	Type*	Architecture	HOMO/VB Level (eV)	V_{OC} (V)	J_{SC} (mA/cm^2)	FF	PCE (%)	Reference PCE (%)	Remark	Ref.
Spiro-OMeTAD	MS	$mpTiO_2/MAPbI_3/HTM$		0.99	20	0.73	15	-	spincoat with LiTFSI, TBP and FK209	[illegible]
	MS	$TiO_2/mpAl_2O_3/MAPbI_{3-x}Cl_x/HTM$	-5.22	1.02	21.5	0.71	15.9	-	spincoat with LiTFSI and TBP	[illegible]
	P	$Y:TiO_2/MAPbI_{3-x}Cl_x/HTM$		1.13	22.8	0.75	19.3	-	spincoat with LiTFSI, TBP and FK209	[illegible]
CuSCN	MS	$mpTiO_2/MAPbI_3/HTM$	-5.3	1.01	19.7	0.62	12.4	-	doctor blading	[illegible]
	P	$TiO_2/MAPbI_{3-x}Cl_x/HTM$		0.73	14.4	0.62	6.4	-	drop cast	[illegible]
NiO	MS	$mpNiO/MAPbI_3/PC_{61}BM/BCP$		0.96	19.8	0.61	11.6	-	low temperature spattering	[illegible]
	P	$HTM/MAPbI_{3-x}Cl_x/PC_{61}BM$	-5.4	0.79	14.2	0.65	7.3	-	electrodeposition	[illegible]
	P	$HTM/MAPbI_3/PC_{61}BM$		0.88	16.3	0.64	9.11	-	sol-gel process	143
Graphene Oxide	P	$HTM/MAPbI_{3-x}Cl_x/PC_{61}BM/ZnO$	-4.9	0.99	15.59	0.72	11.1	9.26 (PEDOT:PSS)	spincoat	139
P3HT	MS	$mpTiO_2/MAPbI_3/HTM$	-5.0-5.2	0.73	12.6	0.73	6.7	8.4 (spiro)	spincoat with LiTFSI and TBP	[illegible]
	P	$TiO_x/MAPbI_{3-x}Cl_x/HTM$		0.98	19.1	0.66	12.4	-	spincoat with LiTFSI and D-TBP	31
PTAA	MS	$mpTiO_2/MAPb(I_{1-x}Br_x)_3/HTM$	-5.14	1.11	19.6	0.74	16.2	-	spincoat with LiTFSI and TBP	[illegible]
PANI	MS	$mpTiO_2/MAPbI_3/HTM$	-5.23	0.78	14.48	0.65	7.34	-	electro polymerization	96
PIF8-TAA	MS	$mpTiO_2/MAPbBr_3/HTM$	-5.51	1.4	6.1	0.79	6.7	-	spincoat with LiTFSI and TBP	99
PEDOT:PSS	P	$HTM/MAPbI_{3-x}Cl_x/PC_{61}BM/PFN$	-4.9-5.2	1.05	20.3	0.80	17.1	-	spincoat	57
PyC	MS	$mpTiO_2/MAPbI_3/HTM$	-5.11	0.89	20.2	0.69	12.4	12.7 (spiro)	spincoat with LiTFSI, TBP and FK209	[illegible]
H101	MS	$mpTiO_2/MAPbI_3/HTM$	-5.16	1.05	19.1	0.65	13.2	13.7 (spiro)	spincoat with LiTFSI, TBP and FK102	102
T103	MS	$mpTiO_2/MAPbI_3/HTM$	-5.33	0.99	20.3	0.62	12.4	12.9 (spiro)	spincoat with LiTFSI, TBP and FK102	[illegible]
po-Spiro OMeTAD	MS	$mpTiO_2/MAPbI_3/HTM$	-5.22	1.02	21.2	0.78	16.7	15.2 (spiro)	spincoat with LiTFSI and TBP	105
OMeTPA-FA	MS	$mpTiO_2/MAPbI_3/HTM$	-5.14	0.97	21	0.67	13.6	14.7 (spiro)	spincoat with LiTFSI, TBP and FK209	106
TTF-1	MS	$mpTiO_2/MAPbI_3/HTM$	-5.05	0.86	19.9	0.64	11	11.4 (spiro)	spincoat	[illegible]
fusedF	MS	$mpTiO_2/MAPbI_3/HTM$	-5.23	1.04	17.9	0.68	12.8	11.7 (spiro)	spincoat	[illegible]
DR3TBDTT	P	$TiO_2/MAPbI_{3-x}Cl_x/HTM$	-5.39	0.95	15.3	0.6	8.8	8.9 (spiro)	spincoat with PDMS	133
HTM-free	MS	$mpTiO_2/MAPbI_3/Au$	-	0.84	19	0.68	10.9	-		114
HTM-free	MS	$mpTiO_2/ZrO_2/(5\text{-}AVA)_x(MA)_{1-x}PbI_3/C$	-	0.86	22.8	0.66	12.8	-		[illegible]

* MS refers to device with mesoscopic architecture and P refers to device with planar architecture.

3.2 Planar architecture

Although the embodiment of sub-150 °C processing has been recently reported for mesoscopic perovskite solar cells *via* the utilization of nanoparticles,[11,83,124] most literature reports still employ mesoporous films that require high-temperature sintering (~ 500 °C), particularly for the most efficient devices. Therefore the lack of mesoporous metal-oxide scaffold contributes to the low-temperature processability of planar heterojunction (PHJ) perovskite solar cells, inevitably imparting the possibility of fabricating flexible solar cells on polyethylene terephthlate (PET) substrates compared to their mesoscopic counterparts. By taking the advantage of low-

temperature processibility, planar perovskite devices can also be integrated into tandem solar cells as top and/or bottom cell. In addition, the scaffold-less planar architecture offers considerable versatility in deposition techniques of organometal halide perovskite, which further widens the options of materials as charge-selective transporting (or blocking) layers to couple with the respective perovskite. The other merit of PHJ solar cells is that they can be employed as testbeds to verify the efficacy of novel materials owing to their simple and versatile preparation. This section provides a summary of reports on various materials, both organic and inorganic, employed as charge-selective transporting (or blocking) layers and interlayers in two types of planar-heterojunction perovskite solar cells, *i.e.*, conventional and inverted architectures (Fig. 5).

3.2.1 Conventional "*n-i-p*" planar perovskite solar cells

The "*n-i-p*" planar architecture strongly inherits the features of the most commonly used mesoscopic perovskite devices (FTO/TiO_2/perovskite/spiro-OMeTAD/Au); hence the term "conventional". Essentially an *n*-type electron selective layer is deposited on a transparent conductive substrate, followed by sequential coating of hybrid perovskite layer, *p*-type hole selective layer and top metal contact (light first passes through the bottom electron selective layer). The main difference with the corresponding mesoscopic devices is the use of a single compact *n*-type metal oxide layer rather than a combination of both compact and mesostructured scaffolds. Planar perovskite solar cells with such configuration have been shown to boast high efficiencies, comparable to their mesoscopic counterparts.[5,17,18]

Electron-transporting materials. Mesoporous TiO_2 (~ 300 nm) layer is often to be reported to be essential for high efficiency perovskite solar cells. This requirement may not be as critical looking at the result of substituting this mp-TiO_2 layer with a thinner layer with much lower

porosity.[8,35,99] Dar *et al.* employed (001)-oriented anatase TiO_2 nanoplatelets to replace the mesoporous scaffold and were able to obtain PCE of 12.3% after thickness optimization of both the $CH_3NH_3PbI_3$ and TiO_2 electron-transporting layers (ETLs).[125] This study implies that under optimized fabrication conditions, reduced porosity has marginal influence on the achievable performance; and with this in mind, planar devices with no porosity should also perform reasonably.

TiO_2 nanoparticles prepared using low-temperature sol-gel synthesis can be used as ETL for PHJ perovskite solar cells.[126] Device with this ETL (ITO/TiO_2/$CH_3NH_3PbI_{3-x}Cl_x$/P3HT/Ag) was able to achieve a PCE of 13.6% and this is strongly dependent on the thermal history of TiO_2. The thermal annealing of compact TiO_2 layer (< 150 °C) is proposed to remove residual impurities and to improve interparticle connectivity. Nevertheless, prolonged heat treatment results in a coarser morphology inducing highly detrimental effects on device performance. Yella *et al.* also demonstrated a low-temperature fabrication of TiO_2/$CH_3NH_3PbI_3$/spiro-OMeTAD PHJ solar cells by utilizing nanocrystalline rutile TiO_2 deposited *via* chemical bath deposition from $TiCl_4$ precursors.[127] The thickness and morphology of the rutile TiO_2 nanoparticles can be adjusted by controlling the concentration of the precursor solution. Under optimized conditions, this rutile TiO_2 PHJ device resulted in an impressive PCE of 13.7% in contrast to 3.7% produced by anatase TiO_2 prepared by spincoating of $TiCl_4$ precursors. The rutile TiO_2 device also exhibits an exceptionally high V_{OC} of 1.11 V. This discrepancy is attributed to the formation of a more intimate contact between rutile TiO_2 and the overlaying perovskite layer, resulting in a more effective extraction of photogenerated electrons.

Besides TiO_2, other *n*-type metal oxides (*e.g.*, ZnO), which have been applied in various mesoscopic perovskite devices, can also be incorporated into planar solar cells.[70,71] Liu and Kelly

reported the use of a low-temperature-processible ZnO thin film as an electron-transporting layer in planar $CH_3NH_3PbI_3$ perovskite devices, demonstrating a PCE as high as 15.7% under AM 1.5G illumination.[18] The higher electron mobility of ZnO compared to TiO_2 renders it a better ETL material.[128] The ZnO nanoparticles prepared *via* hydrolysis of $Zn(O_2CCH_3)_2$ precursor require no thermal treatment and can be readily deposited on conductive substrates. The planar devices fabricated are also highly reproducible with high V_{OC} in excess of 1.0 V. The II-VI (*e.g.*, CdSe) nanoparticles can also be used as electron-transporting layer in perovskite solar cells as demonstrated by Wang *et al.*[129] The low-temperature solution-processed CdSe/$CH_3NH_3PbI_3$/spiro-OMeTAD/Ag planar device yielded PCE of 11.7%.

Hole-transporting material. As discussed previously, organic molecules such as spiro-OMeTAD, are often employed as hole-transporting material (HTM) for both dye-sensitized and mesoscopic perovskite solar cells. Spiro-OMeTAD remains the most popular choice as HTM for conventional planar perovskite solar cells, which enables the attainment of devices with high efficiencies.[5,17,18] Conings *et al.* demonstrated a PCE as high as 10.4% can be achieved from solar cells based on mixed-halide lead perovskites sandwiched between charge-selective contacts of TiO_2 and P3HT.[130] The crystallinity of P3HT can be improved with D-TBP instead of the commonly used TBP, as reported by Guo *et al.* (a PCE of 9.2% for pristine P3HT and a PCE of 12.4% for modified P3HT).[131] Their study highlights that semicrystalline polymers such as polythiophene derivatives are energetically and electronically compatible with perovskite materials, and can thus be alternatives to the amorphous small molecules such as spiro-OMeTAD. Inorganic material CuSCN was also applied as HTM in planar perovskite device showing a PCE of 6.4%.[132]

Zheng *et al.* demonstrated another embodiment of planar architecture by employing a highly hydrophobic oligothiophene derivative (DR3TBDTT) as HTM for PHJ perovskite solar cell without any of the usual ionic additive such as Li-TFSI or *t*BP.[133] Instead, polydimethylsiloxane (PDMS) was used as a morphological control agent to assist the formation of a continuous and uniform HTM layer. The device showed decent performance (PCE = 8.8%) comparable to a device prepared with spiro-OMeTAD + ionic additive (8.9%), with a much improved device stability owing to the moisture resistivity of the oligothiophene molecule.

Interlayer. A few materials have been applied as interlayers in conventional "*n-i-p*" PHJ perovskite solar cells: ethoxylated polyethylenimine (PEIE) and $PC_{61}BM$. Such an interlayer is expected to assist charge injection and extraction at metal-semiconductor interfaces, which in turn have significant impact on the device performance, *via* formation of a quasi-ohmic interfacial contact. The strategy of incorporating an interlayer has led to devices with high fill factors and low series resistance. Zhou *et al.* engineered the interface by inserting a thin layer of PEIE to reduce the work function of the ITO layer from 4.6 to 4.0 eV.[5] It is possible to modify the work function with this interlayer because of the introduction of molecular dipole interactions and this leads to a better match with the conduction band minimum (CBM) of the yttrium-doped TiO_2 electron-transporting layer. In terms of device performance, the insertion of PEIE interlayer manifests itself by a higher photocurrent and fill factor. Another example of interface engineering was shown by Kim *et al.*[134] A $PC_{61}BM$ layer was inserted between ZnO ETL and $CH_3NH_3PbI_3$ layer and the presence of this fullerene-derivative layer alters the electronic structure of the ZnO layer, effectively suppresses the recombination at the ETL-perovskite interface. This eventually leads to a PCE as high as 12.2%, which is about 30% higher than devices without any $PC_{61}BM$ interlayer.

3.2.2 Inverted "*p-i-n*" planar perovskite solar cells

The first few papers employing inverted "*p-i-n*" architecture are based on a solution-processible organolead halide perovskite sandwiched between a *p*-type conducting polymer (PEDOT:PSS) and an *n*-type fullerene derivative ($PC_{61}BM$), with a PEDOT:PSS layer coated directly on the transparent conductive substrate.[15,33] The initial material selection was made with the assumption that the perovskite has good *p*-type characteristics and heavily influenced by the *p-n* heterojunction concept in organic solar cells.[135] PHJ devices with this architecture have also experienced significant performance enhancement in a very short time, from a PCE of mere 3.9% to more than 15%.

Hole-transporting material. Some HTMs that have been used in inverted planar-heterojunction perovskite solar cells include PEDOT:PSS,[15,33,136] polythiophene,[137] spiro-OMeTAD,[138] graphene oxide (GO),[139] NiO,[140-143] V_2O_5[140] and CuSCN.[141] Even though PEDOT:PSS is one of the most commonly used HTMs for inverted planar architecture, its work function is highly dependent on the ratio of its ionomers (~ 4.9–5.2 eV), which may be not be high enough and may not perfectly match the valence band maxima (VBM) of perovskite materials (*e.g.*, –5.4 eV for $CH_3NH_3PbI_3$). Lim *et al.* demonstrated that PEDOT:PSS work function could be tuned by adding a perfluorinated ionomer (PFI) into the polymer solution.[136] The PFI was found to enrich the surface of PEDOT:PSS, resulting in a deeper work function. In terms of device performance, the interface engineering with PFI gave PCE of 11.7%, more than 40% higher than the device without any PFI treatment.

Electrochemically polymerized polythiophene (PT) film was also used as hole-transporting layer in ITO/PT/$CH_3NH_3PbI_3$/C_{60}/BCP/Ag PHJ solar cells due to its matching HOMO level (–5.2 eV)

with the VBM of perovskite materials.[137] The devices exhibit strong correlation between performance and PT film thickness, since PT conductivity tends to increase with thicker films but its strong optical absorption may contribute to loss of photons that can be absorbed by the perovskite layer. Upon PT thickness optimization, a promising PCE of 11.8% was obtained.

In an attempt to correlate the HOMO level of hole-transporting materials with the V_{OC} of solar cells, Polander *et al.* utilized inverted planar architecture with a series of HTMs (HOMO levels ranging from –5.0 to –5.6 eV).[138] Reducing HOMO levels initially leads to an improved device performance, particularly V_{OC}, with the best device with spiro-TTB (HOMO level = –5.3 eV) having methyl groups instead of methoxy groups on spiro-OMeTAD, demonstrating PCE of 10.9% and V_{OC} of 1.03 V. HTMs with HOMO levels lower than –5.3 eV were found to demonstrate poor performance due to the absence of sufficient driving force.

Graphene oxide (GO) is another alternative to PEDOT:PSS. As demonstrated by Wu *et al*., GO films were found to quench the photoluminescence of $CH_3NH_3PbI_{3-x}Cl_x$, suggesting feasibility of charge transfer between the materials; the degree of quenching varied depending on the GO thickness.[139] Furthermore, due to the different surface chemistry, perovskite films formed on GO had better uniformity with fewer pores and improved roughness as compared to those formed on PEDOT:PSS. As a result, GO promotes a better surface coverage and enhanced light scattering, which leads to a better PCE of 11.1% (*vs.* 9.3% for PEDOT:PSS). This is another indication that promoting nucleation is important for good film formation and better coverage as GO provides a hydrophilic surface which reduces the energy barrier for heterogeneous nucleation to occur.

Since PEDOT:PSS is highly hygroscopic, which may compromise the long-term stability of perovskite devices, it is higher desirable to find alternative materials; inorganic metal oxides are ideal choices for this purpose since they are more stable in nature. Docampo *et al.* were among

the first to apply NiO as hole-transporting layer in inverted planar devices but without success, attributed mainly to poor perovskite film formation and poor surface coverage.[140] Later development showed that it is possible to achieve efficiency as high as 9% with NiO. There are various techniques techniques employed to prepare NiO film for PHJ perovskite solar cells: electrodeposition and sol-gel synthesis.[36,141-143] Subbiah *et al.* used an electrodeposited NiO film with vacuum-deposited hybrid perovskite film (FTO/NiO/$CH_3NH_3PbI_{3-x}Cl_x$/ $PC_{61}BM$ /Ag) and achieved a PCE of 7.3%.[141] Jeng *et al.* applied a thin NiO_x hole-transporting layer and observed a better performance with a higher V_{OC} compared to devices prepared with PEDOT:PSS.[142] UV-ozone treatment of NiO_x was found to improve surface wetting properties and energy alignment between NiO_x and perovskite, leading to more than 1.5 times enhancement in device performance (PCE = 7.8%). Similar conclusions on the effect of UV-ozone were reached by Hu *et al*.[36] By using nanocrystals prepared *via* sol-gel method, Zhu *et al.* were able to obtain compact, continuous and corrugated crystalline NiO film with better charge extraction and transport properties compared to PEDOT:PSS.[143] The surface texture of NiO assists the formation of large $CH_3NH_3PbI_3$ crystals with improved light-scattering properties. Consequently, following NiO thickness optimization, PHJ perovskite device with PCE of 9.11% was achieved, much higher as compared to devices with unstructured NiO thin film or with PEDOT:PSS.

Electron-transporting material. Fullerene (C_{60}) and its derivatives are the most widely use *n*-type materials for ETL in inverted perovskite solar cells. We have previously demonstrated that $PC_{61}BM$, one of the more commonly used fullerene derivatives, could effectively quench the photoluminescence of $CH_3NH_3PbI_3$, suggesting a high probability of efficient charge transfer.[15] It remains debatable whether the presence of fullerene is necessary to form the heterojunction required for dissociating the photogenerated excitons formed in perovskite bulk film or whether

the fullerene functions only as a charge extraction and transport layer for the charge-carriers already formed in the perovskite (*i.e.*, fullerene acting as electron acceptor with reference to electron-donating perovskite). Different fullerene derivatives typically possess distinctive solubilities in organic solvents and different optoelectronic properties (*e.g.*, electron mobility and energy level). In terms of the device characteristics, it is imperative to optimize the fullerene film thickness to maximize the attainable PCE. Seo *et al.* demonstrated that a $PC_{61}BM$ layer as thick as ~ 50 nm was sufficient to attain full coverage of the perovskite film, while thicker fullerene layers tended to increase series resistance and modulate light absorption.[144] Apart from $PC_{61}BM$, there are other fullerene compounds have been used in similar device configurations: C_{60}, ICBA and $PC_{71}BM$. Some of the ETL materials and a comparison of their energy levels with the other layers in perovskite solar cells are shown in Fig. 10 and Fig. 11. In an earlier work by Jeng *et al.* on inverted PHJ solar cells with fullerene derivatives, it was shown that devices with $PC_{61}BM$ still outperformed those prepared with C_{60} and ICBA.[33] Nevertheless, the correlation between the LUMO level of the fullerenes and device photovoltage can be established. The lower LUMO level of C_{60} compared to $PC_{61}BM$ (–4.5 eV *vs.* –3.9 eV) corresponds well with the V_{OC} drop in the solar cell devices. On the other hand, cell prepared with ICBA, which has a higher LUMO level than $PC_{61}BM$ (0.17 eV higher), exhibits a higher V_{OC}. Wang *et al.* also made similar observations in terms of the photovoltage trend with the three fullerene derivatives in their planar devices; maximum V_{OC} of 0.53, 0.91 and 1.06 V for C_{60}, $PC_{61}BM$ and ICBA, respectively.[52] By optimizing the deposition conditions of the perovskite film and incorporating additional C_{60} as interlayer, they were able to obtain device with PCE of 12.2% with ICBA. The use of $PC_{71}BM$ to substitute $PC_{61}BM$ was demonstrated by Chiang *et al*.[22] The higher electron mobility and the better optical absorption in the UV-visible range may have contributed to the higher photocurrent

in $PC_{71}BM$ devices. Solvent annealing of $PC_{71}BM$ layer, accomplished by keeping the sample in a solvent-saturated environment, for 24 h was deemed necessary to improve interfacial contact between $PC_{71}BM$ and perovskite layers, as well as to enhance $PC_{71}BM$ crystallinity. As a result, the optimized device employing the higher fullerene exhibited 30% improvement in PCE; its best device performing with PCE of 16.31%.

It is also desirable to find alternative materials to the fullerene family. Malinkiewicz *et al.* showed that organoborane compounds (*e.g.*, 3TPYMB) might be a suitable ETL for PHJ perovskite solar cell.[145] Devices fabricated with 3TPYMB resulted in PCE of 5.5% compared to 10% for $PC_{61}BM$-based device. Nevertheless, it was also noted that the LUMO level of 3TPYMB was higher than that of $PC_{61}BM$ by 0.6 eV. Therefore, there is an offset between CBM of $CH_3NH_3PbI_3$ and LUMO level of 3TPYMB that may inhibit electron transfer, resulting in inferior J_{SC} and V_{OC}. It was also likely that the suboptimal morphology of the organoborane layer contained pinholes that might act as shunting pathways. Further fine-tuning of the energy levels of organoborane as well as optimizing its film morphology may result in more suitable ETL candidates for organometal halide perovskites.

N-type metal oxide such as ZnO has also been tested in planar device with "*p-i-n*" configuration. You *et al.* prepared ITO/PEDOT:PSS/$CH_3NH_3PbI_{3-x}Cl_x$/ZnO/Al device by depositing ZnO nanoparticles from an orthogonal solvent (chlorobenzene). The device showed remarkable efficiency of 11.5%, commensurate with that of $PC_{61}BM$ as ETL, with external quantum efficiency peaking at ~ 80%.[146]

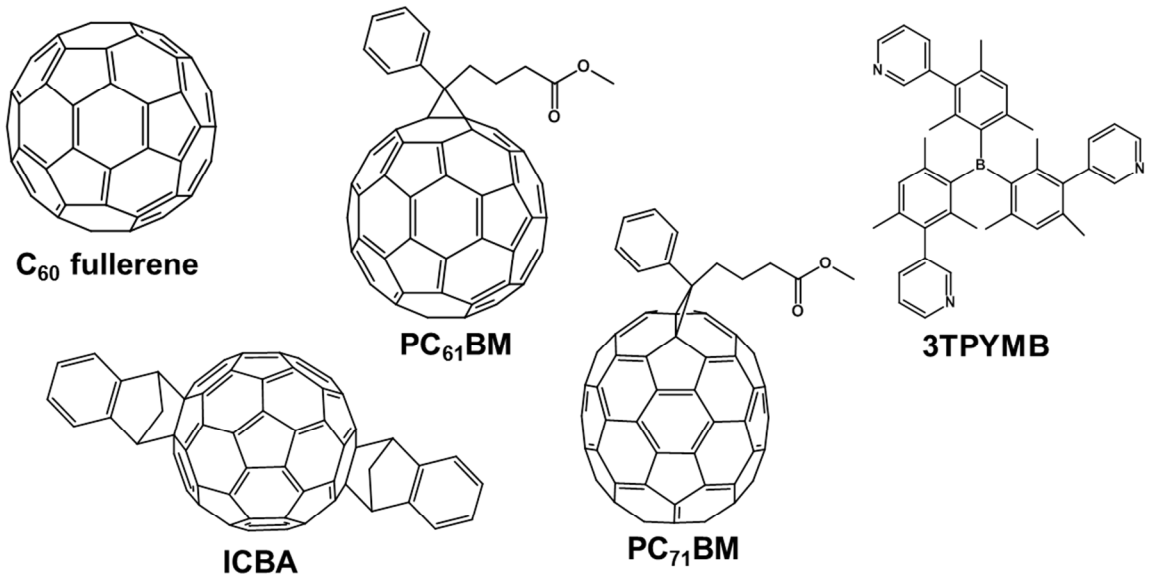

Fig. 10 Structures of some of the ETL materials for perovskite solar cells.

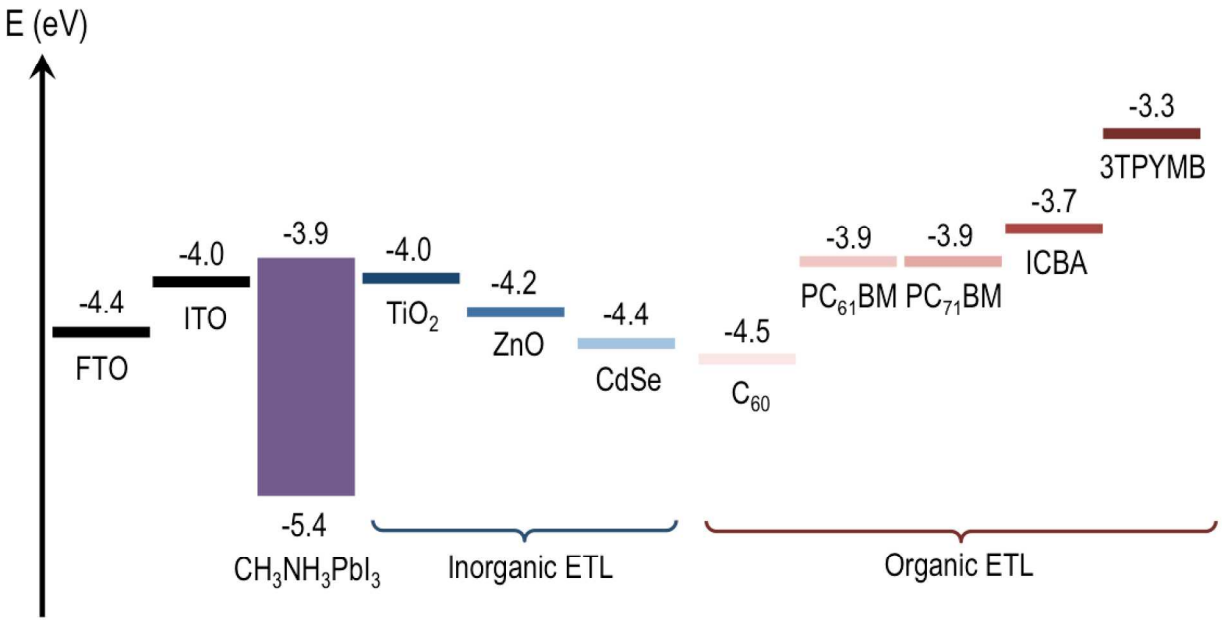

Fig. 11 Energy level diagram showing conduction band/LUMO levels of various ETLs.

Interlayer. There are two types of interlayers demonstrated thus far for inverted planar architecture: *p*-type and *n*-type interlayers (the former is to be inserted close to the hole-transporting layer, while the latter is to be coupled with the electron-transporting layer).

Malinkiewicz *et al.* inserted a thin layer (10–20 nm) of organic polymer poly(*N,N'*-bis(4-butylphenyl)-*N,N'*-bis(phenyl)benzidine) (polyTPD) between PEDOT:PSS and $CH_3NH_3PbI_3$ layers using a meniscus-coating process.[145,147] The roles of polyTPD are two-fold: (1) to assist hole transfer from $CH_3NH_3PbI_3$ to PEDOT:PSS because the HOMO level of polyTPD and the VBM of $CH_3NH_3PbI_3$ are very similar in energy (–5.4 eV), and (2) to block the flow of electrons, which indirectly also promotes the electron drifting to the opposite electrode, since the LUMO level of polyTPD (–2.4 eV) is much closer to vacuum compared with the CBM of $CH_3NH_3PbI_3$ (–3.9 eV). They further discovered that the conductivity of polyTPD played a crucial role for thicker $CH_3NH_3PbI_3$ films.[148] Perovskite films with various thicknesses were prepared (160 to 900 nm) with dual-source thermal evaporation method, providing high control over film uniformity and thickness accuracy, as well as similar morphologies across the different films. The best device was obtained with a 285-nm-thick perovskite film (PCE = 12.7%), while the 900-nm-thick film yielded poorer performance (PCE = 7.2%). Nevertheless, such thickness-dependent behavior was not observed when the polyTPD interlayer was slightly oxidized (or doped) with $AgSbF_6$. With the polyTPD with improved conductivity, the 900-nm-thick $CH_3NH_3PbI_3$ planar device could generate PCE as high as 12%. The study also points out that charge-carrier diffusion lengths, measured to be in the range of ~ 100 nm in past studies on $CH_3NH_3PbI_3$, are dependent on the perovskite film preparation. It is also likely that the high film quality obtained *via* vacuum deposition significantly improves the diffusion lengths; hence, film thickness no longer becomes the main limiting factor for the device performance.

A number of materials have been demonstrated as functional *n*-type interlayers in "*p-i-n*" planar heterojunction devices, namely LiF,[144] bathocuproine (BCP),[33,52] bathophenantroline (BPhen),[38] ZnO,[139] TiO_2,[140,149] Ca,[38,150] C_{60} and its derivatives[32,52] and polyelectrolytes.[151] Most of these

compounds have been previously applied as interlayers in organic solar cells. They are typically incorporated between the electron-transporting layer (*e.g.*, $PC_{61}BM$) and the top electrode. The insertion of thin LiF (~ 0.5 nm), reported by Seo *et al.*, results in simultaneous improvement in both J_{SC} and FF.[144] The presence of LiF generates dipole moment across the interfaces, which in turn reduces the energy barrier between the LUMO level of $PC_{61}BM$ and the Fermi level of Al, resulting in a better electron extraction across both materials.

BCP is a widely used electron-blocking/hole-transporting layer in organic light emitting diodes and organic solar cells. There are a few roles assumed by BCP: (1) improving optical field; leading to increased absorption in the photoactive layer; (2) blocking holes due to its poor hole mobility and its deep HOMO level (–7.0 eV); (3) transporting electrons due to its high electron mobility and its matching energy (LUMO) level with those of fullerene and electrode, and (4) protecting the fullerene layer beneath from damage incurred from electrode deposition. BPhen has similar characteristics to BCP, although the higher electron mobility in BPhen may facilitate a more efficient charge extraction and transport across the interlayer to the electrode.[152]

Double fullerene layers, *i.e.*, a stack of two layers of fullerene or its derivatives, have been employed as an effective measure to reduce device leakage. Wang *et al.* showed that the insertion of a thermally evaporated C_{60} layer on a solution-deposited C_{60} dramatically reduced the dark current in the devices.[52] This indicates the crucial role of the additional C_{60} layer in preventing current leakage. In addition, a double fullerene $C_{60}/PC_{61}BM$ layer was found to passivate the defects (or reduce the trap densities) at both the surface and grain boundaries of the perovskite. A similar concept was also employed by Liang *et al.* by using a solution-processible bis-C_{60} surfactant between the $PC_{61}BM$ HTL and the top Ag electrode.[32] The fullerene (bis-C_{60}) interlayer facilitates the energy alignment at the HTL/electrode interface.

The possibility of exploiting the surface dipole has made polyelectrolyte a suitable choice as interlayer in planar heterojunction solar cells. Zhang *et al.* applied two types of solution-processible polyelectrolytes, *i.e.,* PEIE and poly[3-(6-trimethylammoniumhexyl)thiophene) (P3TMAHT), in devices based on ITO/PEDOT:PSS/$CH_3NH_3PbI_{3-x}Cl_x$/$PC_{61}BM$/interlayer/Ag.[151] Both polymers were found to decrease work function of Ag from 4.7 eV to 3.97 and 4.13 eV, for PEIE and P3TMAHT, respectively, thereby lowering the electron injection barrier at the $PC_{61}BM$/Ag interface. Consequently, the devices improved from 8.5% (without interlayer) to 12.0% (with PEIE) and 11.3% (with P3TMAHT).

3.3 Mesoscopic versus planar architectures

Undeterred by their humble beginnings, solid-state organolead halide hybrid perovskite solar cells with planar heterojunction architecture have undergone a dramatic development over the past few years. As discussed previously, up until now the optimization of the thin-film planar perovskite devices have led to outstanding efficiencies in excess of 15%, very comparable to or in some cases even better than their mesoscopic equivalents, thus opening the unavoidable discussion of the merits of the planar and mesoscopic perovskite cells. The simplicity of the planar heterojunction suggests that it is a more technologically viable architecture to adopt and very good large-scale manufacturability. Leijtens *et al.* compared the electronic properties of both architectures and found that the planar perovskite films were superior in terms of charge carrier mobility (> 20 cm^2 V^{-1} s^{-1}). However, solar cells prepared with planar configuration suffered from photovoltage loss, which could be due to the high density of traps states in planar solar cells resulting in high non-radiative electron-hole recombination.[153] Passivation or

elimination of electronic trap sites in the organic-inorganic lead halide perovskites, for instance, *via* Lewis base passivation as shown by Noel *et al*., can lead to higher V_{OC} in planar perovskite solar cells.[21] Other than manufacturability and electrical mobility, there are other characteristics of the films/device that are influenced by the architecture of the cells. In the following sections, a comparison between the impact of the architectures on the different critical aspects of the cells will be discussed.

3.3.1 Morphology and crystallization

As discussed in an earlier section, the perovskite film morphology depends strongly on the crystallization process involved. Compared to a planar substrate, a mesoporous scaffold with higher surface area tends to promote a more extensive heterogeneous nucleation, which leads to the formation of smaller crystallites. Such a distinction was observed by Ball *et al*.[11] $CH_3NH_3PbI_{3-x}Cl_x$ perovskite film prepared on a flat TiO_2 layer was found to have crystals larger than 500 nm and the size of the crystals is reduced to 60–100 nm when deposited entirely within a mesoporous Al_2O_3 scaffold (Fig. 12). Both polycrystalline films exhibit distinct absorption spectra; the spectra of the smaller crystallites in the mesoporous scaffold show broader and hypsochromically shifted absorption spectra with respect to films deposited on the flat substrates.[154,155] Despite the larger crystal size, which is generally more desirable for an efficient charge transport, it is much more arduous to prepare excellent perovskite films on planar substrates. Nevertheless, various methods have been devised to meet this challenge, as summarized in the previous morphology section. In the case of organolead halide perovskites, highly efficient devices have been observed with polycrystalline films over a range of certain grain sizes, suggesting long charge-carrier diffusion lengths and harmless grain boundaries.[17,35]

In fact, as measured by Oga *et al*., the minimum mobilities in $CH_3NH_3PbI_3$ films with various crystallite sizes (70–420 nm) range between 10 and 20 $cm^2\ V^{-1}\ s^{-1}$.[156] Apart from the crystallite size, another concern that needs to be addressed to enable production of devices with high efficiencies includes crystallite quality (presence of defects within or on the surface of the crystals) and crystal orientation (specific direction for better charge transport).

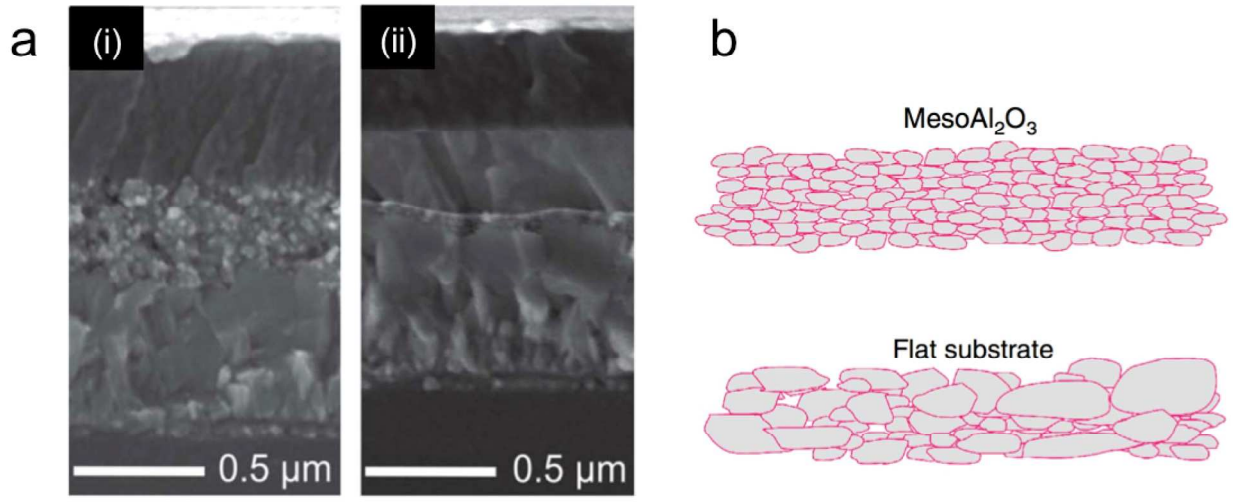

Fig. 12 (a) Cross-sectional SEM micrographs of solar cells with (i) Al_2O_3 scaffold and (ii) no scaffold,[11] (b) schematic representation of the average crystals dimension for samples deposited on an Al_2O_3 scaffold (top) and on a flat substrate (bottom).[154]

The other issue with mesoscopic cells that does not exist for planar architecture is incomplete pore filling. The nanoscale morphology of perovskite-filled TiO_2 scaffold can be probed visually with analytical TEM techniques, *e.g.,* electron energy loss spectroscopy (EELS) and electron spectroscopy imaging (ESI) as was first demonstrated by Nanova *et al*.[157] Leijtens *et al.* pointed out that incomplete pore filling of TiO_2 scaffold with perovskite material could cause an unwanted contact between *p*-type HTM and *n*-type TiO_2.[68] By reducing the thickness of mesoporous TiO_2 scaffold, they were able to improve the PCE from 6.3% to 8.6%, as improved

pore filling could be attained and following that, the formation of a perovskite capping layer. Other than optimizing the thickness and porosity of the scaffold, pore filling can be enhanced by improving solution viscosity, applying a longer infiltration time prior to deposition or by improving the surface properties of the scaffold.

3.3.2 Film thickness, diffusion length and charge-carrier generation

One main disadvantage associated with planar architecture proposed in the early stages of the development of perovskite solar cells is that the device performance would be critically constrained by exciton and free carrier diffusion lengths. Early reports also suggested that perovskite solar cells are excitonic in nature; this means charge carriers are only generated upon exciton dissociation across heterointerfaces.[158] In the event of insufficiently long exciton and free carrier diffusion lengths, a planar solar cell constructed with a thick absorber film, which is typically required to maximize photoabsorption, is expected to suffer from poor performance. The mesoscopic architecture offers a solution to this problem by enabling maximum absorption without sacrificing exciton and charge recombination. Another solution is to use perovskite materials with longer diffusion lengths; $CH_3NH_3PbI_{3-x}Cl_x$, for instance, has electron-hole diffusion lengths in excess of 1 μm while the triiodide ($CH_3NH_3PbI_3$) perovskite has diffusion lengths of only ~ 100 nm.[13,14]

Nevertheless, at present even $CH_3NH_3PbI_3$ perovskite films with thickness approaching 1 μm have been employed in highly efficient planar heterojunction solar cells.[25,148] These results raise the question of whether there is a need to reassess the diffusion lengths and further elucidate the working mechanism in perovskite solar cells. As revealed by Edri *et al.*, solar cell based on perovskite sandwiched between hole- and electron-transporting layers, operate as a "*p-i-n*"

device regardless of the device architecture.[87] There are two strong electron beam-induced current (EBIC) signals near the "*p*" and "*n*" regions, suggesting strong charge separation and collection at both interfaces with charge-selective transporting layers. The presence of the internal field in the "*i*" region could assist charge-carrier drift. Docampo *et al.* proposed that the electron-hole diffusion length could be dependent on the method employed in the film preparation, which consequently might affect the film morphology.[23] They obtained diffusion lengths of ~ 200 nm for $CH_3NH_3PbI_3$ perovskite prepared by solution-based sequential deposition. A much higher value of close to 1 μm was estimated by Edri *et al*. in a separate EBIC study.[123] They argued that such variation could arise as their measurement was performed on the complete device, as opposed to only the thin film, in which internal electric field induced by selective contacts might influence the photoelectrical processes in the measured sample. Given the low exciton binding energy of organolead halide perovskite, the excitons may also dissociate into free carriers in the bulk, lifting the limitation imposed by exciton diffusion length.[154] While there is still no consensus on the exciton binding energy, it was found that free carriers accumulating at the band-edge of the hybrid perovskite $CH_3NH_3PbI_3$ could promote a further reduction in the exciton binding energy *via* coulombic screening of photogenerated excitons, which enhances the formation of free carriers in the bulk.[159] In fact, in a theoretical investigation performed by Even *et al*., it was suggested that the complete screening of the Wannier-Mott excitons at room temperature, which was induced by the optical phonons and collective rotational motion of the organic cations, could lead to almost free carriers.[160] To conclude this section, the mesoscopic device is thus the preferred choice for materials with short diffusion lengths due to the smaller distance the excitons/free carriers have to travel, which in turn also depends on the pore sizes in the scaffold.

3.3.3 Hysteresis

Anomalous *I-V* hysteresis phenomena, *i.e.*, variations in the *I-V* characteristics depending on the direction and the rate of voltage sweep, was observed for perovskite solar cells and this posed a great concern as they undermine the accurary of the measured efficiencies of these devices.[161] The photocurrent appears to be dependent on the bias voltage applied just before the measurement is performed; hence the device can be "pre-conditioned". Therefore, a voltage sweep in the direction of open circuit to short circuit tends to artificially enhance the current measured. The origin of hysteresis is still open to debate, although defects and polarizability of the perovskite have been proposed as possible reasons. The use of a mesoporous TiO_2 scaffold significantly impairs the hysteresis effects, while the corresponding planar devices suffer from severe hysteresis (Fig. 13).[29,162-164] Kim and Park discovered that the low-frequency capacitance was higher in a planar device, suggesting that a planar substrate could induce dipole polarization in $CH_3NH_3PbI_3$ perovskite film, which was attributed to be the cause of the hysteresis.[162] On the other hand, Snaith *et al.* proposed that the severity of hysteresis was dependent on the quality of interface between perovskite and the charge-selective contacts.[163] Due to the higher surface area, charge transfer between perovskite and mesoporous TiO_2 scaffold is more efficient, resulting in diminished impact of the phenomenon. Hysteresis could still be observed in cells fabricated with a mesoporous "passive" insulating Al_2O_3 scaffold. Noel *et al.* demonstrated that the hysteresis of a planar device could be reduced by passivating the surface defects of the perovskite layer with treatments of pyridine or thiophene.[21]

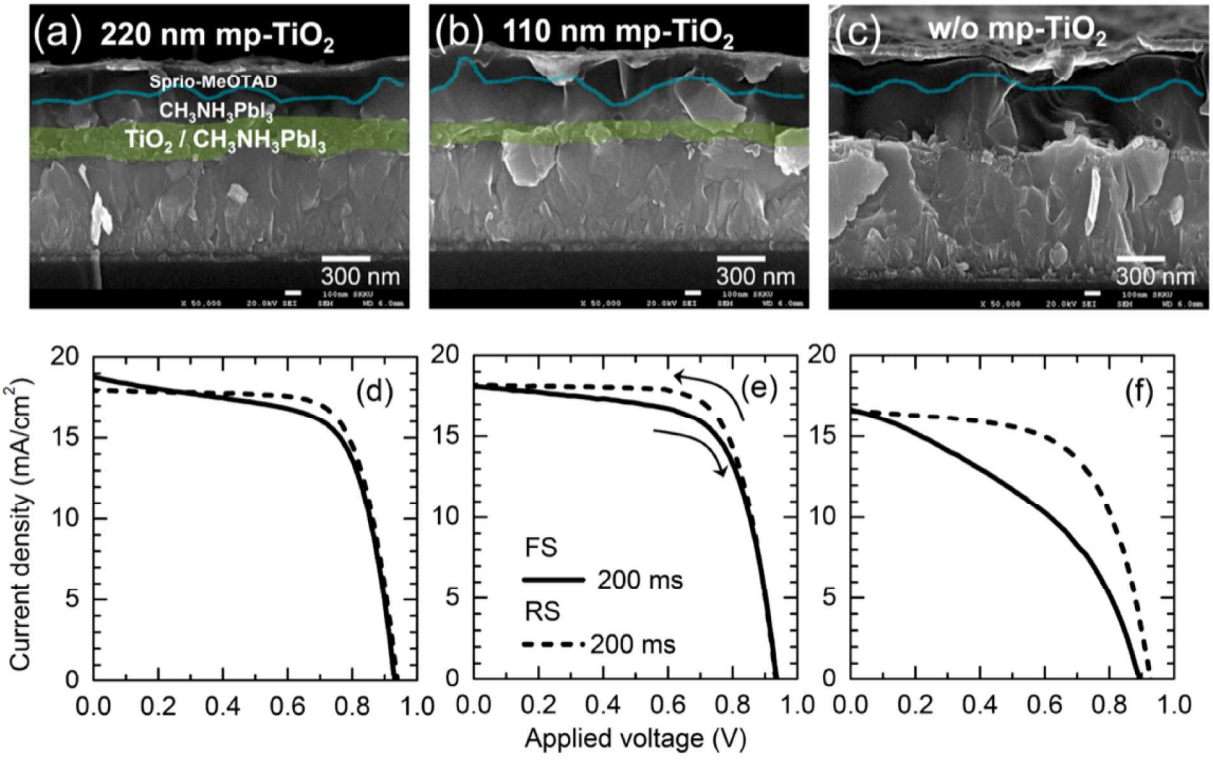

Fig. 13 Cross-sectional SEM images of $CH_3NH_3PbI_3$ devices with (a) 220 and (b) 110 nm thick mp-TiO_2 and (c) planar device without mp-TiO_2. *I–V* curves measured at FS (solid line) and RS (dashed line) for mesostructured devices with (d) 220 and (e) 110 thick mp-TiO_2 and (f) planar device without mp-TiO_2.[162]

We surmise that the device architecture is not the inherent root cause of the hysteresis observed. While a mesoporous TiO_2 scaffold appears to be successful in attenuating hysteresis, it is clear that this is not so for an Al_2O_3 scaffold. Even the degree of hysteresis varies depending on the thickness of the mesoporous TiO_2.[163] Interestingly, inverted planar perovskite devices based on PEDOT:PSS/perovskite/$PC_{61}BM$ with high efficiencies have been reported without any observed hysteresis.[19,22,25] We also note that the photoluminescence quenching of $CH_3NH_3PbI_{3-x}Cl_x$ with PEDOT:PSS and $PC_{61}BM$ is more efficient than with spiro-OMeTAD and TiO_2, respectively.[140] This can be translated into a more efficient hole transfer from the perovskite layer to

PEDOT:PSS than to spiro-OMeTAD and a more efficient electron transfer from the perovskite layer to $PC_{61}BM$ than to TiO_2. Extrapolating from the conclusion given by Snaith *et al.* on the impact of interface quality, we believe that inverted perovskite device with this material combination is less likely to develop hysteresis and that a hysteresis-free could be even obtained from a conventional "*n-i-p*" device with the appropriate materials as charge-selective contacts.[163] As such, the hysteresis issue could be overcome by proper material selection and, to a certain extent, morphology optimization notwithstanding the type of device architecture.

3.3.4 PbI_2 contribution

It has been previously demonstrated that PbI_2 formed upon the decomposition of organolead halide perovskites.[53] For reasons that are not yet fully understood, the formation of a PbI_2 phase is more prominent in hybrid perovskite samples prepared on a mesoporous scaffold than on a planar substrate.[155] Due to its wide bandgap (E_g = 2.3 eV), the presence of PbI_2 species is commonly undesirable because of its poorer optical absorption properties than those of $CH_3NH_3PbI_3$. Mesoscopic solar cell devices prepared with PbI_2 (FTO/c-TiO_2/mp-TiO_2/PbI_2/spiro-OMeTAD/Ag) have demonstrated poor performance, attributing to its significantly inferior transport properties (smaller diffusion coefficient) to those of $CH_3NH_3PbI_3$-based devices.[165] PbI_2 forming in a perovskite film, as in the case of an over-annealed perovskite film, might cause energy misalignment at TiO_2 interface and it could also trap free charges generated in the perovskite phase, leading to a deteriorated device.

The notion of a detrimental PbI_2 phase is not shared by everyone, as it has also been proposed that a tiny amount of PbI_2 can lead to self-passivation of the defect states in the perovskite film and charge selectivity at the perovskite interface.[166,167] Chen *et al.* observed the formation of PbI_2

species along the grain boundaries, although extended annealing resulted in the conversion of whole perovskite grains.[108] There are three plausible roles of PbI_2 in self-passivating $CH_3NH_3PbI_3$: (1) to preclude excitons from surface defects due to the type I energy alignment; (2) to reduce recombination between electrons from TiO_2 and holes from perovskite at interface I, and (3) to reduce recombination between electrons from perovskite and holes from hole-transporting material (HTM) (Fig. 14). The presence of a small amount of PbI_2 in perovskite film also increases carrier lifetimes, leading to improved device performances.[108,155] As compared to planar devices, mesoscopic perovskite solar cell may be more easily self-passivated due to the higher chance for PbI_2 formation. However, this may also lead to adverse effects if too much PbI_2 phase is present, imposing more stringent requirements on the processing of these thin films.

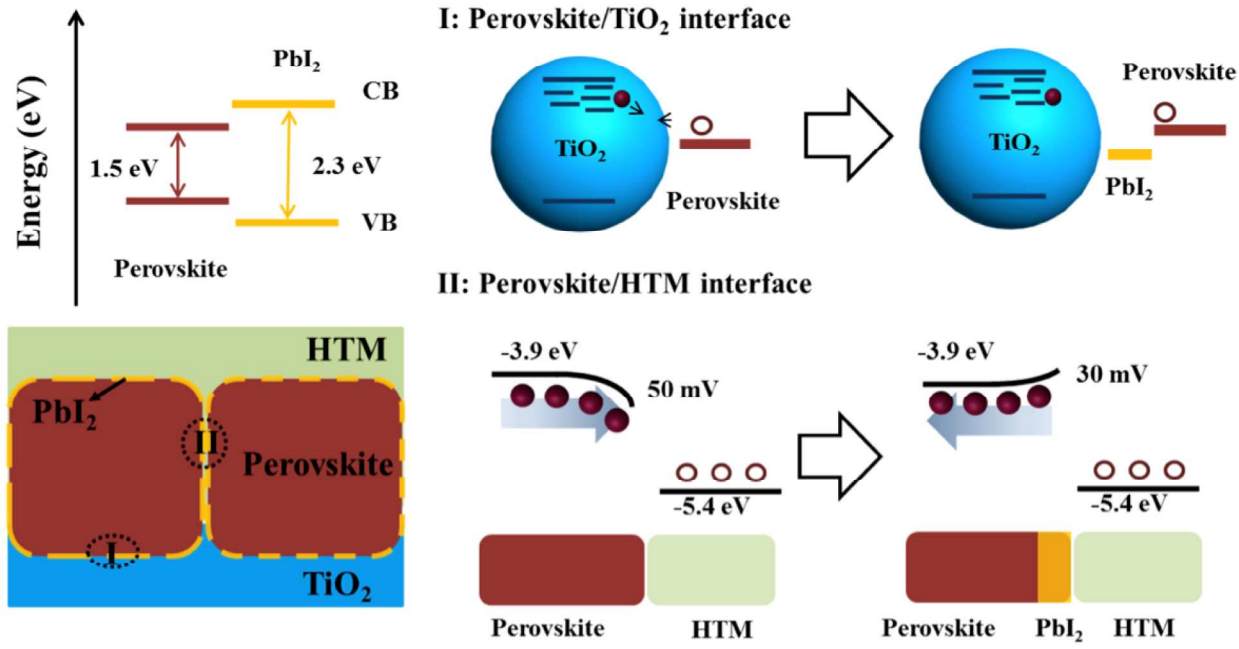

Fig. 14 Schematics of proposed mechanism of self-passivation of PbI_2 in $CH_3NH_3PbI_3$ film.[108]

4. Material and device stability

Perovskite solar cells have undoubtedly demonstrated the possibility of attaining excitingly high efficiencies comparable to those obtained for thin-film solar cells in the foreseeable future. It is still confronted by a very crucial challenge before any worldwide acceptance and commercial viability can be established, and that is the long-term environmental stability (air, moisture and thermal stability) of the devices that is largely dependent on the choice of materials. Organometal halide perovskites are intrinsically susceptible to moisture and heat, while the organics in the cells tend to degrade in the presence of moisture, oxygen and heat. The instability of lead halide perovskite (*e.g.*, $CH_3NH_3PbI_3$) in humid environment is often reflected by the decrease in film absorption between 530 and 800 nm, as reported by Niu *et al.*[168] The moisture-induced degradation of $CH_3NH_3PbI_3$ is also evident from the disappearance of the XRD peaks relating to the initial perovskite structure and the emergence of peaks corresponding to the degradation products comprising PbI_2 and I_2; the formation of I_2 is triggered only when both moisture and light are present. Habisreutinger *et al.* also pointed out that the color change from dark brown/black to yellow in lead halide perovskite films upon degradation in air could be attributed to the bond dissociation among the crystal units induced by the reaction between water molecules and the highly hygroscopic methylammonium cations, resulting in the transformation of the perovskite crystal structure to a lower dimensional system.[95] Therefore, perovskite solar cells entail stringent encapsulation to ensure a long outdoor operational lifetime.

Despite the pressing issue and the huge interest in device stabiliy, the number of published studies on long-term device stability remains scarce. The first work on long-term stability of perovskite solar cell was reported by Kim *et al.* demonstrating stable performance over 500 h, although the study was only done ex-situ, *i.e.,* devices were stored in air at room temperature and

were only intermittently measured under AM 1.5G illumination.[8] The precise conditions for ageing studies of perovskite solar cells remain unclear and therefore need to be standardized. To resolve this ambiguity, Grätzel recommended long-term stability tests for encapsulated devices that include light-soaking tests (1000 h in full sunlight) and damp heat tests (1000 h at 85%RH and 85 °C).[169] A highly promising long-term device stability was obtained by Burschka *et al.* demonstrating an encapsulated mesoscopic perovskite solar cell (FTO/c-TiO_2/mp-TiO_2/$CH_3NH_3PbI_3$/spiro-OMeTAD/Au) that only degraded to approximately 80% of its initial efficiency after being light-soaked (~ 100 mW/cm^2 at 45 °C) for 500 h.[35] The absence of any significant change in the device photocurrent after the testing period suggests that the perovskite material remains photochemically stable under encapsulation. Law *et al.* also demonstrated that sealed perovskite solar cell with similar architecture only suffered from an 8% decrease in photocurrent under continuous high-intensity illumination (equivalent to ~ 40 Sun) for > 60 h.[170] Nevertheless, a much poorer stability was observed upon substitution of spiro-OMeTAD with the other HTMs (*e.g.*, P3HT and DPPTTT), replacement of mp-TiO_2 scaffold with mp-Al_2O_3 and when encapsulation was not employed.

Leitjens *et al.* argued that stability study had to be realized under simulated solar illumination instead of white light emitting diodes (LEDs) that was devoid of ultraviolet (UV) component,[171] under which the abovementioned studies by Burschka *et al.* and Law *et al.* were performed.[35,170] They discovered that under AM1.5G (1 sun) illumination the encapsulated FTO/c-TiO_2/mp-TiO_2/$CH_3NH_3PbI_{3-x}Cl_x$/spiro-OMeTAD/Au device degraded to < 10% of its initial efficiency within 5 h, while the corresponding UV-filtered device decayed to only ~ 85% of its initial performance. Oxygen molecules in the air tend to be adsorbed on the oxygen vacancies on TiO_2 surface. It was hypothesized that upon UV light excitation, the photogenerated holes in the

valence band could recombine with the electrons at oxygen vacancies at the TiO_2 surface, leaving free electrons in the conduction band and generating unfilled oxygen vacancy sites (Fig. 15). These deep electronic sites could further trap the photogenerated electrons, from which they could recombine with holes in the HTM, which results in the instability of the UV-aged perovskite solar cells. To circumvent the inherent UV-induced instability of TiO_2-based solar cells, Leitjens *et al.* proposed the use of insulating Al_2O_3 to substitute the TiO_2 scaffold. Expectedly, the TiO_2-free system demonstrated a much-enhanced stability with a decrease of ~ 50% of its initial efficiency within the first 200 h of exposure and an impressive stabilized PCE at ~ 6% over 1000 h of continuous AM 1.5G illumination without any UV filter.

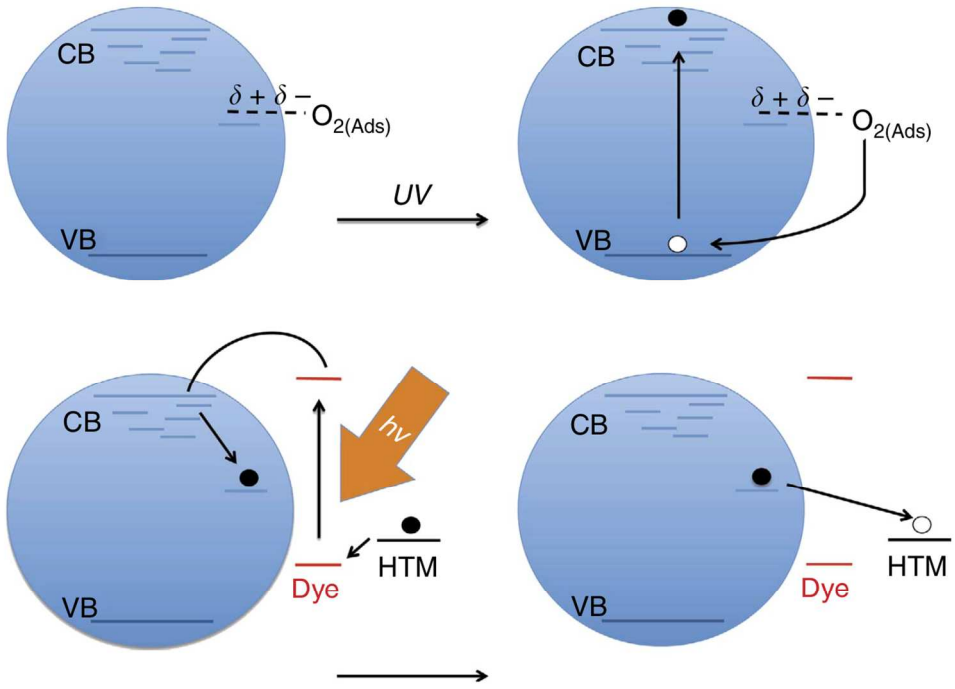

Fig. 15 Schematics of proposed mechanism of UV-induced degradation in TiO_2-based solar cell.[171]

The long-term stability of perovskite solar cells can also be improved by employing additional barrier layers to protect the perovskite film beneath, in addition to external encapsulation strategies. The efficacy of such protection largely depends on gas permeability and hydrophobicity of the "moisture-shielding" layer. Habisreutinger *et al.* substituted organic HTMs with a carbon nanotube–PMMA composite, demonstrating an enhanced stability of the protected organolead halide perovskite of up to ~ 100 h at 80 °C.[95] This is evident from the lack of change in the absorption spectra and crystal structure of the perovskite since the hydrophobic PMMA is expected to prevent the permeation of water molecules. Improvement in moisture stability was also attained upon insertion of a thin Al_2O_3 barrier layer between $CH_3NH_3PbI_3$ and spiro-OMeTAD layers.[168] Upon exposure to humidity of 60% at 35 °C, the device with Al_2O_3 incorporation demonstrated a drop of ~ 50% of its initial efficiency in contrast with a decrease of ~ 80% within 18 h. Moisture barrier can also be extended by employing moisture-impermeable counter electrode even in the absence of HTM layer. The use of a thick carbon electrode (~10 μm) in the HTM-free perovskite solar cell, discussed earlier in section 3.1.4, remarkably improved its long-term stability, *i.e.,* no apparent decrease in device PCE, under AM 1.5G illumination in air over 1000 h without any encapsulation.[120] The other strategy to improve moisture stability is by using HTMs with higher hydrophobicity, thus preventing water infiltration into the perovskite layer. In an ex-situ stability test at 20% humidity, unsealed perovskite solar cell with a HTM based on hydrophobic polymer was shown to keep its PCE stable for 1000 h, while the corresponding device with spiro-OMeTAD as its HTM showed 28% reduction in PCE.[100] Device stability can be further improved by eliminating the incorporation of highly hygroscopic ionic additives, *e.g.,* Li-TFSI, commonly expected to improve hole mobility,

in conjunction with the use of hydrophobic HTM with high mobility.[133] Furthermore, the choice of HTM additive is also expected to affect the long-term stability of perovskite solar cells.[172]

Besides moisture stability, thermal stability is another fundamental concern since continuous exposure to light illumination (*e.g.*, 100 mW/cm^2 in full sun) may heat up the solar cells, raising their operating temperature to as high as 80 °C.[173] This may exacerbate any moisture-induced degradation processes already present in the devices. Organolead halide hybrid perovskites have been reported to degrade into its original lead halide precursors as the more unstable organohalide components decompose under heating. Although metal halide perovskite materials have been reported to be stable up above 300 °C,[92,174,175] recent work demonstrate that the decomposition of the organic component occurs at temperatures much lower than 300 °C, even as low as 140 °C.[53,166,176] As discussed earlier in section 3.3.4, the presence of metal halide (*e.g.*, PbI_2) as degradation product of the hybrid perovskite (*e.g.*, $CH_3NH_3PbI_3$) may interfere with the electrical processes in perovskite solar cells due to their inferior electrical properties and incompatible bandgap alignment. These lead halides may also possess poor photon harvesting capability. On the other hand, the thermal decomposition of organohalide (*e.g.*, CH_3NH_3I) may lead to the formation of hydrogen halide (*e.g.*, HI) and amine compound (*e.g.*, CH_3NH_2); the latter tends to remain more persistently within the perovskite matrix, subsequently affecting the photoconversion processes.[176] The thermal stability of perovskite solar cells can be improved by either employing impervious barrier films to prevent the organic components from escaping or utilizing new perovskite materials with better inherent thermal stability.[95,177]

In summary, other than competitive efficiencies, robust solar cells with excellent moisture and thermal stabilities are highly sought for. As discussed in the earlier section, the presence of "mild" moisture can in fact assist the formation of perovskite film with larger grain size and

reduced pinholes.[5,57] Different approaches to improve device stability developed thus far have mainly emphasized on the incorporation of barrier films in various forms. Nevertheless, it is more crucial, in our opinion, to develop materials with novel chemistries that are less susceptible to moisture and prolonged heating. The use of mixed halide, for instance, is a viable method to engineer perovskite materials with enhanced stability.[178] Device architecture, which remains ambiguous in terms of its effects on the device stability, should also be considered when performing future long-term stability tests.

5. Summary

The comparison of the merits of each of the architecture is inevitable as mesoscopic and planar perovskite devices, derived from very different origins (dye-sensitized solar cells *vs.* thin-film solar cells), have achieved similarly excellent efficiencies. The reason for such universal good performances is most probably the forgiving optoelectronic properties offered by this class of material (high absorption coefficient, bandgap compatible to solar spectrum, excellent charge lifetimes and good charge mobilities). That being said, the rapid development of this field only took off in 2013 and the reason for this is that there was then a common recognition and acceptance of the importance of controlled crystallization in these films. Hence in this review, the two important factors contributing to the spectacular or, in some cases, the lack of spectacular performance in perovskite solar cells – morphology of the perovskite films and the architecture of the cells – are discussed. Many different physical and chemical methods have been used to control the crystallization process with various degree of success. The better control has led to reasonable performance achieved in both architectures. That being said, mesoporous architectures provide a simple and straightforward way to achieved controllable crystallization

with good surface finish. However, the preparation of the mesoporous scaffold also requires a careful selection of materials, hence limiting the material options available for this type of architecture. Due to their low-temperature processibility, planar heterojunction perovskite solar cells are better suited for fabrication on flexible polymer substrates. Thus far flexible planar devices have demonstrated high efficiencies approaching 10%.[18,136,146] Commercially attractive semitransparent solar cells can be more easily implemented with planar configuration as "solar windows" for buildings and vehicles. Perovskite materials are ideal for this purpose due to their high optical absorption even with reasonably thin films and tunability of the optical transmittance by controlling the film morphology.[179,180] The other key advantage of planar heterojunction over mesoscopic architecture is its simple fabrication, rendering it a more viable option as the platform to evaluate the potential of novel materials and more intricate multijunction architectures.[181,182] The high charge mobility and versatility offered by planar architectures is offset by the limit in the photovoltage due to presence of sub gap states and low intrinsic doping densities.[153] For highly efficient solar cells, a combination of both planar and mesoscopic architecture may eventually be the way to go forward. Regardless of the architecture forward, lowering the energy for nucleation and controlled growth in these films will lead to the better solar cells performance.

References

1. K. Chondroudis and D. B. Mitzi, *Chemistry of Materials*, 1999, **11,** 3028-3030.
2. D. B. Mitzi, *Prog Inorg Chem*, 1999, **48,** 1-121.
3. D. B. Mitzi, C. A. Feild, Z. Schlesinger and R. B. Laibowitz, *J Solid State Chem*, 1995, **114,** 159-163.

4. A. Kojima, K. Teshima, Y. Shirai and T. Miyasaka, *J. Am. Chem. Soc.*, 2009, **131,** 6050-6051.

5. H. Zhou, Q. Chen, G. Li, S. Luo, T.-b. Song, H.-S. Duan, Z. Hong, J. You, Y. Liu and Y. Yang, *Science*, 2014, **345,** 542-546.

6. J.-H. Im, C.-R. Lee, J.-W. Lee, S.-W. Park and N.-G. Park, *Nanoscale*, 2011, **3,** 4088-4093.

7. M. M. Lee, J. Teuscher, T. Miyasaka, T. N. Murakami and H. J. Snaith, *Science*, 2012, **338,** 643-647.

8. H.-S. Kim, C.-R. Lee, J.-H. Im, K.-B. Lee, T. Moehl, A. Marchioro, S.-J. Moon, R. Humphry-Baker, J.-H. Yum, J. E. Moser, M. Gratzel and N.-G. Park, *Sci. Rep.*, 2012, **2**.

9. M. A. Green, *J. Mater. Sci. Mater. Electron.*, 2007, **18,** 15-19.

10. P. Kovacik, G. Sforazzini, A. G. Cook, S. M. Willis, P. S. Grant, H. E. Assender and A. A. R. Watt, *ACS Appl. Mater. Interfaces*, 2010, **3,** 11-15.

11. J. M. Ball, M. M. Lee, A. Hey and H. J. Snaith, *Energy Environ. Sci.*, 2013, **6,** 1739-1743.

12. J. M. Frost, K. T. Butler, F. Brivio, C. H. Hendon, M. van Schilfgaarde and A. Walsh, *Nano Lett.*, 2014, **14,** 2584-2590.

13. S. D. Stranks, G. E. Eperon, G. Grancini, C. Menelaou, M. J. P. Alcocer, T. Leijtens, L. M. Herz, A. Petrozza and H. J. Snaith, *Science*, 2013, **342,** 341-344.

14. G. Xing, N. Mathews, S. Sun, S. S. Lim, Y. M. Lam, M. Grätzel, S. Mhaisalkar and T. C. Sum, *Science*, 2013, **342,** 344-347.

15. S. Sun, T. Salim, N. Mathews, M. Duchamp, C. Boothroyd, G. Xing, T. C. Sum and Y. M. Lam, *Energy Environ. Sci.*, 2014, **7,** 399-407.

16. W.-J. Yin, T. Shi and Y. Yan, *Adv. Mater.*, 2014, **26,** 4653-4658.

17. M. Liu, M. B. Johnston and H. J. Snaith, *Nature*, 2013, **501,** 395-398.

18. D. Liu and T. L. Kelly, *Nat. Photon.*, 2014, **8,** 133-138.

19. Z. Xiao, C. Bi, Y. Shao, Q. Dong, Q. Wang, Y. Yuan, C. Wang, Y. Gao and J. Huang, *Energy Environ. Sci.*, 2014, **7,** 2619-2623.

20. M. Xiao, F. Huang, W. Huang, Y. Dkhissi, Y. Zhu, J. Etheridge, A. Gray-Weale, U. Bach, Y.-B. Cheng and L. Spiccia, *Angew. Chem. Int. Ed.*, 2014, **53,** 9898-9903.

21. N. K. Noel, A. Abate, S. D. Stranks, E. Parrott, V. Burlakov, A. Goriely and H. J. Snaith, *ACS Nano*, 2014, **8,** 9815-9821.

22. C.-H. Chiang, Z.-L. Tseng and C.-G. Wu, *J. Mater. Chem. A*, 2014, **2,** 15897-15903.

23. P. Docampo, F. Hanusch, S. D. Stranks, M. Döblinger, J. M. Feckl, M. Ehrensperger, N. K. Minar, M. B. Johnston, H. J. Snaith and T. Bein, *Adv. Energy Mater.*, 2014, **4**.

24. F. Huang, Y. Dkhissi, W. Huang, M. Xiao, I. Benesperi, S. Rubanov, Y. Zhu, X. Lin, L. Jiang, Y. Zhou, A. Gray-Weale, J. Etheridge, C. R. McNeill, R. A. Caruso, U. Bach, L. Spiccia and Y.-B. Cheng, *Nano Energy*, 2014, **10,** 10-18.

25. Z. Xiao, Q. Dong, C. Bi, Y. Shao, Y. Yuan and J. Huang, *Adv. Mater.*, 2014, **26,** 6503-6509.

26. S. Gamliel and L. Etgar, *RSC Adv.*, 2014, **4,** 29012-29021.

27. M. He, D. Zheng, M. Wang, C. Lin and Z. Lin, *J. Mater. Chem. A*, 2014, **2,** 5994-6003.

28. G. E. Eperon, V. M. Burlakov, P. Docampo, A. Goriely and H. J. Snaith, *Adv. Funct. Mater.*, 2014, **24,** 151-157.

29. N. J. Jeon, J. H. Noh, Y. C. Kim, W. S. Yang, S. Ryu and S. I. Seok, *Nat. Mater.*, 2014, **13,** 897-903.

30. J. C. Maxwell, *Philos Mag*, 1908, **16,** 818-824.

31. D. Yang, M. Krasowska, R. Sedev and J. Ralston, *Phys. Chem. Chem. Phys.*, 2010, **12,** 13724-13729.

32. P.-W. Liang, C.-Y. Liao, C.-C. Chueh, F. Zuo, S. T. Williams, X.-K. Xin, J. Lin and A. K. Y. Jen, *Adv. Mater.*, 2014, **26,** 3748-3754.

33. J.-Y. Jeng, Y.-F. Chiang, M.-H. Lee, S.-R. Peng, T.-F. Guo, P. Chen and T.-C. Wen, *Adv. Mater.*, 2013, **25,** 3727-3732.

34. Y.-F. Chiang, J.-Y. Jeng, M.-H. Lee, S.-R. Peng, P. Chen, T.-F. Guo, T.-C. Wen, Y.-J. Hsu and C.-M. Hsu, *Phys. Chem. Chem. Phys.*, 2014, **16,** 6033-6040.

35. J. Burschka, N. Pellet, S.-J. Moon, R. Humphry-Baker, P. Gao, M. K. Nazeeruddin and M. Gratzel, *Nature*, 2013, **499,** 316-319.

36. L. Hu, J. Peng, W. Wang, Z. Xia, J. Yuan, J. Lu, X. Huang, W. Ma, H. Song, W. Chen, Y.-B. Cheng and J. Tang, *ACS Photonics*, 2014, **1,** 547-553.

37. H. Hu, D. Wang, Y. Zhou, J. Zhang, S. Lv, S. Pang, X. Chen, Z. Liu, N. P. Padture and G. Cui, *RSC Adv.*, 2014, **4,** 28964-28967.

38. C.-W. Chen, H.-W. Kang, S.-Y. Hsiao, P.-F. Yang, K.-M. Chiang and H.-W. Lin, *Adv. Mater.*, 2014, **26,** 6647-6652.

39. Q. Chen, H. Zhou, Z. Hong, S. Luo, H.-S. Duan, H.-H. Wang, Y. Liu, G. Li and Y. Yang, *J. Am. Chem. Soc.*, 2013, **136,** 622-625.

40. H.-B. Kim, H. Choi, J. Jeong, S. Kim, B. Walker, S. Song and J. Y. Kim, *Nanoscale*, 2014, **6,** 6679-6683.

41. Y. Wu, A. Islam, X. Yang, C. Qin, J. Liu, K. Zhang, W. Peng and L. Han, *Energy Environ. Sci.*, 2014, **7,** 2934-2938.

42. Y. Zhao and K. Zhu, *J. Phys. Chem. C*, 2014, **118,** 9412-9418.

43. H. Yu, F. Wang, F. Xie, W. Li, J. Chen and N. Zhao, *Adv. Funct. Mater.*, 2014, **24,** 7102-7108.

44. P.-W. Liang, C.-C. Chueh, X.-K. Xin, F. Zuo, S. T. Williams, C.-Y. Liao and A. K. Y. Jen, *Adv. Energy Mater.*, 2014, DOI: 10.1002/aenm.201400960.

45. Y. Zhao and K. Zhu, *J. Am. Chem. Soc.*, 2014, **136,** 12241-12244.

46. C. Zuo and L. Ding, *Nanoscale*, 2014, **6,** 9935-9938.

47. K. W. Tan, D. T. Moore, M. Saliba, H. Sai, L. A. Estroff, T. Hanrath, H. J. Snaith and U. Wiesner, *ACS Nano*, 2014, **8,** 4730-4739.

48. Y. Tidhar, E. Edri, H. Weissman, D. Zohar, G. Hodes, D. Cahen, B. Rybtchinski and S. Kirmayer, *J. Am. Chem. Soc.*, 2014, **136,** 13249-13256.

49. S. T. Williams, F. Zuo, C.-C. Chueh, C.-Y. Liao, P.-W. Liang and A. K. Y. Jen, *ACS Nano*, 2014, **8,** 10640-10654.

50. M. H. Du, *J. Mater. Chem. A*, 2014, **2,** 9091-9098.

51. E. Mosconi, E. Ronca and F. De Angelis, *J. Phys. Chem. Lett.*, 2014, **5,** 2619-2625.

52. Q. Wang, Y. Shao, Q. Dong, Z. Xiao, Y. Yuan and J. Huang, *Energy Environ. Sci.*, 2014, **7,** 2359-2365.

53. A. Dualeh, N. Tétreault, T. Moehl, P. Gao, M. K. Nazeeruddin and M. Grätzel, *Adv. Funct. Mater.*, 2014, **24,** 3250-3258.

54. M. Saliba, K. W. Tan, H. Sai, D. T. Moore, T. Scott, W. Zhang, L. A. Estroff, U. Wiesner and H. J. Snaith, *J. Phys. Chem. C*, 2014, **118,** 17171-17177.

55. H.-L. Hsu, C.-P. Chen, J.-Y. Chang, Y.-Y. Yu and Y.-K. Shen, *Nanoscale*, 2014, **6,** 10281-10288.

56. G. Li, Y. Yao, H. Yang, V. Shrotriya, G. Yang and Y. Yang, *Adv. Funct. Mater.*, 2007, **17,** 1636-1644.

57. J. You, Y. Yang, Z. Hong, T.-B. Song, L. Meng, Y. Liu, C. Jiang, H. Zhou, W.-H. Chang, G. Li and Y. Yang, *Appl. Phys. Lett.*, 2014, **105,** 183902.

58. J. H. Rhee, C.-C. Chung and E. W.-G. Diau, *NPG Asia Mater.*, 2013, **5,** e68.

59. N.-G. Park, *The Journal of Physical Chemistry Letters*, 2013, **4,** 2423-2429.

60. H.-S. Kim, S. H. Im and N.-G. Park, *J. Phys. Chem. C*, 2014, **118,** 5615-5625.

61. B. Wang, X. Xiao and T. Chen, *Nanoscale*, 2014, **6,** 12287-12297.

62. H. J. Snaith, *J. Phys. Chem. Lett.*, 2013, **4,** 3623-3630.

63. P. P. Boix, K. Nonomura, N. Mathews and S. G. Mhaisalkar, *Mater. Today*, 2014, **17,** 16-23.

64. U. Bach, D. Lupo, P. Comte, J. E. Moser, F. Weissortel, J. Salbeck, H. Spreitzer and M. Gratzel, *Nature*, 1998, **395,** 583-585.

65. T. C. Sum and N. Mathews, *Energy Environ. Sci.*, 2014, **7,** 2518-2534.

66. P. Gao, M. Gratzel and M. K. Nazeeruddin, *Energy Environ. Sci.*, 2014, **7,** 2448-2463.

67. A. Mei, X. Li, L. Liu, Z. Ku, T. Liu, Y. Rong, M. Xu, M. Hu, J. Chen, Y. Yang, M. Gratzel and H. Han, *Science*, 2014, **345,** 295-298.

68. T. Leijtens, B. Lauber, G. E. Eperon, S. D. Stranks and H. J. Snaith, *J. Phys. Chem. Lett.*, 2014, **5,** 1096-1102.

69. D. Bi, G. Boschloo, S. Schwarzmuller, L. Yang, E. M. J. Johansson and A. Hagfeldt, *Nanoscale*, 2013, **5,** 11686-11691.

70. M. H. Kumar, N. Yantara, S. Dharani, M. Graetzel, S. Mhaisalkar, P. P. Boix and N. Mathews, *Chem. Commun.*, 2013, **49,** 11089-11091.

71. D.-Y. Son, J.-H. Im, H.-S. Kim and N.-G. Park, *J. Phys. Chem. C*, 2014, **118,** 16567-16573.

72. X. Gao, J. Li, J. Baker, Y. Hou, D. Guan, J. Chen and C. Yuan, *Chem. Commun.*, 2014, **50,** 6368-6371.

73. J. Qiu, Y. Qiu, K. Yan, M. Zhong, C. Mu, H. Yan and S. Yang, *Nanoscale*, 2013, **5,** 3245-3248.

74. K. Manseki, T. Ikeya, A. Tamura, T. Ban, T. Sugiura and T. Yoshida, *RSC Adv.*, 2014, **4,** 9652-9655.

75. D. Zhong, B. Cai, X. Wang, Z. Yang, Y. Xing, S. Miao, W.-H. Zhang and C. Li, *Nano Energy*, 2015, **11,** 409-418.

76. H. Tian, B. Xu, H. Chen, E. M. J. Johansson and G. Boschloo, *ChemSusChem*, 2014, **7,** 2150-2153.

77. K.-C. Wang, J.-Y. Jeng, P.-S. Shen, Y.-C. Chang, E. W.-G. Diau, C.-H. Tsai, T.-Y. Chao, H.-C. Hsu, P.-Y. Lin, P. Chen, T.-F. Guo and T.-C. Wen, *Sci. Rep.*, 2014, **4**.

78. K.-C. Wang, P.-S. Shen, M.-H. Li, S. Chen, M.-W. Lin, P. Chen and T.-F. Guo, *ACS Appl. Mater. Interfaces*, 2014, **6,** 11851-11858.

79. L. Etgar, P. Gao, P. Qin, M. Graetzel and M. K. Nazeeruddin, *J. Mat. Chem. A*, 2014, **2,** 11586-11590.

80. A. Abrusci, S. D. Stranks, P. Docampo, H.-L. Yip, A. K. Y. Jen and H. J. Snaith, *Nano Lett.*, 2013, **13,** 3124-3128.

81. Z. Zhu, J. Ma, Z. Wang, C. Mu, Z. Fan, L. Du, Y. Bai, L. Fan, H. Yan, D. L. Phillips and S. Yang, *J. Am. Chem. Soc.*, 2014, **136,** 3760-3763.

82. J. T.-W. Wang, J. M. Ball, E. M. Barea, A. Abate, J. A. Alexander-Webber, J. Huang, M. Saliba, I. Mora-Sero, J. Bisquert, H. J. Snaith and R. J. Nicholas, *Nano Lett.*, 2013, **14,** 724-730.

83. K. Wojciechowski, M. Saliba, T. Leijtens, A. Abate and H. J. Snaith, *Energy Environ. Sci.*, 2014, **7,** 1142-1147.

84. D. Bi, S.-J. Moon, L. Haggman, G. Boschloo, L. Yang, E. M. J. Johansson, M. K. Nazeeruddin, M. Gratzel and A. Hagfeldt, *RSC Adv.*, 2013, **3,** 18762-18766.

85. S. H. Hwang, J. Roh, J. Lee, J. Ryu, J. Yun and J. Jang, *J. Mat. Chem. A*, 2014, **2,** 16429-16433.

86. H.-S. Kim, I. Mora-Sero, V. Gonzalez-Pedro, F. Fabregat-Santiago, E. J. Juarez-Perez, N.-G. Park and J. Bisquert, *Nat. Commun.*, 2013, **4**.

87. E. Edri, S. Kirmayer, S. Mukhopadhyay, K. Gartsman, G. Hodes and D. Cahen, *Nat. Commun.*, 2014, **5**.

88. Y. Shirota and H. Kageyama, *Chem. Rev.*, 2007, **107,** 953-1010.

89. J. Burschka, A. Dualeh, F. Kessler, E. Baranoff, N.-L. Cevey-Ha, C. Yi, M. K. Nazeeruddin and M. Grätzel, *J. Am. Chem. Soc.*, 2011, **133,** 18042-18045.

90. J. A. Christians, R. C. M. Fung and P. V. Kamat, *J. Am. Chem. Soc.*, 2013, **136,** 758-764.

91. P. Qin, S. Tanaka, S. Ito, N. Tetreault, K. Manabe, H. Nishino, M. K. Nazeeruddin and M. Grätzel, *Nat Commun*, 2014, **5**.

92. J. H. Heo, S. H. Im, J. H. Noh, T. N. Mandal, C.-S. Lim, J. A. Chang, Y. H. Lee, H.-J. Kim, A. Sarkar, M. K. Nazeeruddin, M. Gratzel and S. I. Seok, *Nat. Photon.*, 2013, **7,** 486-491.

93. M. A. Green, K. Emery, Y. Hishikawa, W. Warta and E. D. Dunlop, *Prog. Photovolt: Res. Appl.*, 2014, **22,** 701-710.

94. H. Chen, X. Pan, W. Liu, M. Cai, D. Kou, Z. Huo, X. Fang and S. Dai, *Chem. Commun.*, 2013, **49,** 7277-7279.

95. S. N. Habisreutinger, T. Leijtens, G. E. Eperon, S. D. Stranks, R. J. Nicholas and H. J. Snaith, *Nano Lett.*, 2014, **14,** 5561-5568.

96. Y. Xiao, G. Han, Y. Chang, H. Zhou, M. Li and Y. Li, *J. Power Sources*, 2014, **267,** 1-8.

97. B. Cai, Y. Xing, Z. Yang, W.-H. Zhang and J. Qiu, *Energy Environ. Sci.*, 2013, **6,** 1480.

98. E. Edri, S. Kirmayer, M. Kulbak, G. Hodes and D. Cahen, *J. Phys. Chem. Lett.*, 2014, **5,** 429-433.

99. S. Ryu, J. H. Noh, N. J. Jeon, Y. Chan Kim, W. S. Yang, J. Seo and S. I. Seok, *Energy Environ. Sci.*, 2014, **7,** 2614-2618.

100. Y. S. Kwon, J. Lim, H.-J. Yun, Y.-H. Kim and T. Park, *Energy Environ. Sci.*, 2014, **7,** 1454.

101. N. J. Jeon, J. Lee, J. H. Noh, M. K. Nazeeruddin, M. Gratzel and S. I. Seok, *J. Am. Chem. Soc.*, 2013, **135,** 19087-19090.

102. H. Li, K. Fu, A. Hagfeldt, M. Gratzel, S. G. Mhaisalkar and A. C. Grimsdale, *Angew. Chem. Int. Ed.*, 2014, **53,** 4085-4088.

103. T. Krishnamoorthy, F. Kunwu, P. P. Boix, H. Li, T. M. Koh, W. L. Leong, S. Powar, A. Grimsdale, M. Gratzel, N. Mathews and S. G. Mhaisalkar, *J. Mat. Chem. A*, 2014, **2,** 6305-6309.

104. A. Krishna, D. Sabba, H. Li, J. Yin, P. P. Boix, C. Soci, S. G. Mhaisalkar and A. C. Grimsdale, *Chem. Sci.*, 2014, **5,** 2702.

105. N. J. Jeon, H. G. Lee, Y. C. Kim, J. Seo, J. H. Noh, J. Lee and S. I. Seok, *J. Am. Chem. Soc.*, 2014, **136,** 7837-7840.

106. H. Choi, S. Paek, N. Lim, Y. H. Lee, M. K. Nazeeruddin and J. Ko, *Chemistry – A European Journal*, 2014, **20,** 10894-10899.

107. J. Wang, S. Wang, X. Li, L. Zhu, Q. Meng, Y. Xiao and D. Li, *Chem. Commun.*, 2014, **50,** 5829-5832.

108. Q. Chen, H. Zhou, T.-B. Song, S. Luo, Z. Hong, H.-S. Duan, L. Dou, Y. Liu and Y. Yang, *Nano Lett.*, 2014, **14,** 4158-4163.

109. P. Qin, S. Paek, M. I. Dar, N. Pellet, J. Ko, M. Gratzel and M. K. Nazeeruddin, *J. Am. Chem. Soc.*, 2014, **136,** 8516-8519.

110. D. Bi, L. Yang, G. Boschloo, A. Hagfeldt and E. M. J. Johansson, *J. Phys. Chem. Lett.*, 2013, **4,** 1532-1536.

111. E. J. Juarez-Perez, M. Wuβler, F. Fabregat-Santiago, K. Lakus-Wollny, E. Mankel, T. Mayer, W. Jaegermann and I. Mora-Sero, *J. Phys. Chem. Lett.*, 2014, **5,** 680-685.

112. L. Etgar, P. Gao, Z. Xue, Q. Peng, A. K. Chandiran, B. Liu, M. K. Nazeeruddin and M. Gratzel, *J. Am. Chem. Soc.*, 2012, **134,** 17396-17399.

113. W. A. Laban and L. Etgar, *Energy Environ. Sci.*, 2013, **6,** 3249.

114. S. Aharon, S. Gamliel, B. E. Cohen and L. Etgar, *Phys. Chem. Chem. Phys.*, 2014, **16,** 10512-10518.

115. J. Shi, J. Dong, S. Lv, Y. Xu, L. Zhu, J. Xiao, X. Xu, H. Wu, D. Li, Y. Luo and Q. Meng, *Appl. Phys. Lett.*, 2014, **104,** 063901.

116. F. Hao, C. C. Stoumpos, Z. Liu, R. P. Chang and M. G. Kanatzidis, *J. Am. Chem. Soc.*, 2014, **136,** 16411-16419.

117. B.-E. Cohen, S. Gamliel and L. Etgar, *APL Mater.*, 2014, **2,** 081502.

118. S. Aharon, B. E. Cohen and L. Etgar, *J. Phys. Chem. C*, 2014, **118,** 17160-17165.

119. Z. Ku, Y. Rong, M. Xu, T. Liu and H. Han, *Sci. Rep.*, 2013, **3,** 3132.

120. A. Mei, X. Li, L. Liu, Z. Ku, T. Liu, Y. Rong, M. Xu, M. Hu, J. Chen, Y. Yang, M. Grätzel and H. Han, *Science*, 2014, **345,** 295-298.

121. M. Xu, Y. Rong, Z. Ku, A. Mei, T. Liu, L. Zhang, X. Li and H. Han, *J. Mat. Chem. A*, 2014, **2,** 8607.

122. Z. Wei, K. Yan, H. Chen, Y. Yi, T. Zhang, X. Long, J. Li, L. Zhang, J. Wang and S. Yang, *Energy Environ. Sci.*, 2014, **7,** 3326-3333.

123. E. Edri, S. Kirmayer, A. Henning, S. Mukhopadhyay, K. Gartsman, Y. Rosenwaks, G. Hodes and D. Cahen, *Nano Lett.*, 2014, **14,** 1000-1004.

124. J.-W. Lee, T.-Y. Lee, P. J. Yoo, M. Gratzel, S. Mhaisalkar and N.-G. Park, *J. Mater. Chem. A*, 2014, **2,** 9251-9259.

125. M. I. Dar, F. J. Ramos, Z. Xue, B. Liu, S. Ahmad, S. A. Shivashankar, M. K. Nazeeruddin and M. Grätzel, *Chem. Mater.*, 2014, **26,** 4675-4678.

126. B. Conings, L. Baeten, T. Jacobs, R. Dera, J. D'Haen, J. Manca and H.-G. Boyen, *APL Mater.*, 2014, **2,** 081505.

127. A. Yella, L.-P. Heiniger, P. Gao, M. K. Nazeeruddin and M. Grätzel, *Nano Lett.*, 2014, **14,** 2591-2596.

128. Q. Zhang, C. S. Dandeneau, X. Zhou and G. Cao, *Adv. Mater.*, 2009, **21,** 4087-4108.

129. L. Wang, W. Fu, Z. Gu, C. Fan, X. Yang, H. Li and H. Chen, *J. Mat. Chem. C*, 2014, **2,** 9087-9090.

130. B. Conings, L. Baeten, C. De Dobbelaere, J. D'Haen, J. Manca and H.-G. Boyen, *Adv. Mater.*, 2014, **26,** 2041-2046.

131. Y. Guo, C. Liu, K. Inoue, K. Harano, H. Tanaka and E. Nakamura, *J. Mat. Chem. A*, 2014, **2,** 13827-13830.

132. S. Chavhan, O. Miguel, H.-J. Grande, V. Gonzalez-Pedro, R. S. Sanchez, E. M. Barea, I. Mora-Sero and R. Tena-Zaera, *J. Mater. Chem. A*, 2014, **2,** 12754-12760.

133. L. Zheng, Y.-H. Chung, Y. Ma, L. Zhang, L. Xiao, Z. Chen, S. Wang, B. Qu and Q. Gong, *Chem. Commun.*, 2014, **50,** 11196-11199.

134. J. Kim, G. Kim, T. K. Kim, S. Kwon, H. Back, J. Lee, S. H. Lee, H. Kang and K. Lee, *J. Mater. Chem. A*, 2014, **2,** 17291-17296.

135. G. Li, R. Zhu and Y. Yang, *Nat. Photon.*, 2012, **6,** 153-161.

136. K.-G. Lim, H.-B. Kim, J. Jeong, H. Kim, J. Y. Kim and T.-W. Lee, *Adv. Mater.*, 2014, **26,** 6461-6466.

137. W. Yan, Y. Li, W. Sun, H. Peng, S. Ye, Z. Liu, Z. Bian and C. Huang, *RSC Adv.*, 2014, **4,** 33039-33046.

138. L. E. Polander, P. Pahner, M. Schwarze, M. Saalfrank, C. Koerner and K. Leo, *APL Mater.*, 2014, **2,** 081503.

139. Z. Wu, S. Bai, J. Xiang, Z. Yuan, Y. Yang, W. Cui, X. Gao, Z. Liu, Y. Jin and B. Sun, *Nanoscale*, 2014, **6,** 10505-10510.

140. P. Docampo, J. M. Ball, M. Darwich, G. E. Eperon and H. J. Snaith, *Nat. Commun.*, 2013, **4**.

141. A. S. Subbiah, A. Halder, S. Ghosh, N. Mahuli, G. Hodes and S. K. Sarkar, *J. Phys. Chem. Lett.*, 2014, **5,** 1748-1753.

142. J.-Y. Jeng, K.-C. Chen, T.-Y. Chiang, P.-Y. Lin, T.-D. Tsai, Y.-C. Chang, T.-F. Guo, P. Chen, T.-C. Wen and Y.-J. Hsu, *Adv. Mater.*, 2014, **26,** 4107-4113.

143. Z. Zhu, Y. Bai, T. Zhang, Z. Liu, X. Long, Z. Wei, Z. Wang, L. Zhang, J. Wang, F. Yan and S. Yang, *Angew. Chem. Int. Ed.*, 2014, **53,** 12571-12575.

144. J. Seo, S. Park, Y. Chan Kim, N. J. Jeon, J. H. Noh, S. C. Yoon and S. I. Seok, *Energy Environ. Sci.*, 2014, **7,** 2642-2646.

145. O. Malinkiewicz, C. Roldán-Carmona, A. Soriano, E. Bandiello, L. Camacho, M. K. Nazeeruddin and H. J. Bolink, *Adv. Energy Mater.*, 2014, DOI: 10.1002/aenm.201400345.

146. J. You, Z. Hong, Y. Yang, Q. Chen, M. Cai, T.-B. Song, C.-C. Chen, S. Lu, Y. Liu, H. Zhou and Y. Yang, *ACS Nano*, 2014, **8,** 1674-1680.

147. O. Malinkiewicz, A. Yella, Y. H. Lee, G. M. Espallargas, M. Graetzel, M. K. Nazeeruddin and H. J. Bolink, *Nat. Photon.*, 2014, **8,** 128-132.

148. C. Momblona, O. Malinkiewicz, C. Roldán-Carmona, A. Soriano, L. Gil-Escrig, E. Bandiello, M. Scheepers, E. Edri and H. J. Bolink, *APL Mater.*, 2014, **2,** 081504.

149. Y.-Y. Yu, R.-S. Chiang, H.-L. Hsu, C.-C. Yang and C.-P. Chen, *Nanoscale*, 2014, **6,** 11403-11410.

150. A. T. Barrows, A. J. Pearson, C. K. Kwak, A. D. F. Dunbar, A. R. Buckley and D. G. Lidzey, *Energy Environ. Sci.*, 2014, **7,** 2944-2950.

151. H. Zhang, H. Azimi, Y. Hou, T. Ameri, T. Przybilla, E. Spiecker, M. Kraft, U. Scherf and C. J. Brabec, *Chem. Mater.*, 2014, **26,** 5190-5193.

152. D. Liu Xiao, S.-L. Zhao, Z. Xu, F.-J. Zhang, T.-H. Zhang, W. Gong, G. Yan, C. Kong, Y.-S. Wang and X.-R. Xu, *Chin. Phys. B*, 2011, **20,** 068801.

153. T. Leijtens, S. D. Stranks, G. E. Eperon, R. Lindblad, E. M. J. Johansson, I. J. McPherson, H. Rensmo, J. M. Ball, M. M. Lee and H. J. Snaith, *ACS Nano*, 2014, **8,** 7147-7155.

154. V. D'Innocenzo, G. Grancini, M. J. P. Alcocer, A. R. S. Kandada, S. D. Stranks, M. M. Lee, G. Lanzani, H. J. Snaith and A. Petrozza, *Nat. Commun.*, 2014, **5**.

155. L. Wang, C. McCleese, A. Kovalsky, Y. Zhao and C. Burda, *J. Am. Chem. Soc.*, 2014, **136,** 12205-12208.

156. H. Oga, A. Saeki, Y. Ogomi, S. Hayase and S. Seki, *J. Am. Chem. Soc.*, 2014, **136,** 13818-13825.

157. D. Nanova, A. K. Kast, M. Pfannmöller, C. Müller, L. Veith, I. Wacker, M. Agari, W. Hermes, P. Erk, W. Kowalsky, R. R. Schröder and R. Lovrinčić, *Nano Lett.*, 2014, **14,** 2735-2740.

158. B. A. Gregg, *J. Phys. Chem. B*, 2003, **107,** 4688-4698.

159. J. S. Manser and P. V. Kamat, *Nat. Photon.*, 2014, **8,** 737-743.

160. J. Even, L. Pedesseau and C. Katan, *J. Phys. Chem. C*, 2014, **118,** 11566-11572.

161. M. D. McGehee, *Nat. Mater.*, 2014, **13,** 845-846.

162. H.-S. Kim and N.-G. Park, *J. Phys. Chem. Lett.*, 2014, **5,** 2927-2934.

163. H. J. Snaith, A. Abate, J. M. Ball, G. E. Eperon, T. Leijtens, N. K. Noel, S. D. Stranks, J. T.-W. Wang, K. Wojciechowski and W. Zhang, *J. Phys. Chem. Lett.*, 2014, **5,** 1511-1515.

164. E. L. Unger, E. T. Hoke, C. D. Bailie, W. H. Nguyen, A. R. Bowring, T. Heumuller, M. G. Christoforo and M. D. McGehee, *Energy Environ. Sci.*, 2014, **7,** 3690-3698.

165. Y. Zhao, A. Nardes and K. Zhu, *Faraday Discuss.*, 2014, DOI: 10.1039/C4FD00128A.

166. T. Supasai, N. Rujisamphan, K. Ullrich, A. Chemseddine and T. Dittrich, *Appl. Phys. Lett.*, 2013, **103,** 183906.

167. V. Somsongkul, F. Lang, A. R. Jeong, M. Rusu, M. Arunchaiya and T. Dittrich, *Phys. Status Solidi RRL*, 2014, **08,** 763-766.

168. G. Niu, W. Li, F. Meng, L. Wang, H. Dong and Y. Qiu, *J. Mat. Chem. A*, 2014, **2,** 705-710.

169. M. Gratzel, *Nat. Mater.*, 2014, **13,** 838-842.

170. C. Law, L. Miseikis, S. Dimitrov, P. Shakya-Tuladhar, X. Li, P. R. F. Barnes, J. Durrant and B. C. O'Regan, *Adv. Mater.*, 2014, **26,** 6268-6273.

171. T. Leijtens, G. E. Eperon, S. Pathak, A. Abate, M. M. Lee and H. J. Snaith, *Nat. Commun.*, 2013, **4**.

172. L. Badia, E. Mas-Marzá, R. S. Sánchez, E. M. Barea, J. Bisquert and I. Mora-Seró, *APL Mater.*, 2014, **2,** 081507.

173. M. Jorgensen, K. Norrman, S. A. Gevorgyan, T. Tromholt, B. Andreasen and F. C. Krebs, *Adv. Mater.*, 2012, **24,** 580-612.

174. C. C. Stoumpos, C. D. Malliakas and M. G. Kanatzidis, *Inorg. Chem.*, 2013, **52,** 9019-9038.

175. T. Baikie, Y. Fang, J. M. Kadro, M. Schreyer, F. Wei, S. G. Mhaisalkar, M. Graetzel and T. J. White, *J. Mat. Chem. A*, 2013, **1,** 5628-5641.

176. A. Dualeh, P. Gao, S. I. Seok, M. K. Nazeeruddin and M. Grätzel, *Chem. Mater.*, 2014, **26,** 6160-6164.

177. S. Aharon, A. Dymshits, A. Rotem and L. Etgar, *J. Mat. Chem. A*, 2015, DOI: 10.1039/C4TA05149A.

178. J. H. Noh, S. H. Im, J. H. Heo, T. N. Mandal and S. I. Seok, *Nano Lett.*, 2013, **13,** 1764-1769.

179. G. E. Eperon, V. M. Burlakov, A. Goriely and H. J. Snaith, *ACS Nano*, 2013, **8,** 591-598.

180. V. M. Burlakov, G. E. Eperon, H. J. Snaith, S. J. Chapman and A. Goriely, *Appl. Phys. Lett.*, 2014, **104,** 091602.

181. H. Choi, J. Jeong, H.-B. Kim, S. Kim, B. Walker, G.-H. Kim and J. Y. Kim, *Nano Energy*, 2014, **7,** 80-85.

182. F. Zuo, S. T. Williams, P.-W. Liang, C.-C. Chueh, C.-Y. Liao and A. K. Y. Jen, *Adv. Mater.*, 2014, **26,** 6454-6460.

Perovskite-Based Solar Cells: Impact of Morphology and Device Architecture on Device Performance

Teddy Salim,[a] Shuangyong Sun,[a] Yuichiro Abe,[a,b] Anurag Krishna,[a,b] Andrew C. Grimsdale[a] and Yeng Ming Lam[a*]

This review provides an overview of factors affecting film morphology and how together with device architecture impact perovskite cells performance.